On the Feasibility of the Hyperloop Concept

by

Yaseem Rana

Submitted to the Department of Mechanical Engineering
in partial fulfillment of the requirements for the degree of

Bachelor of Science in Mechanical Engineering

at the

MASSACHUSETTS INSTITUTE OF TECHNOLOGY

May 2020

Author .....
Department of Mechanical Engineering
May 22, 2020

Certified by .....
Alexander H. Slocum
Walter M. May and A. Hazel May Professor
of Mechanical Engineering
Thesis Supervisor

Accepted by .....
Maria Yang
Undergraduate Officer
Professor of Mechanical Engineering

On the Feasibility of the Hyperloop Concept

by

Yaseem Rana

Submitted to the Department of Mechanical Engineering
on May 22, 2020, in partial fulfillment of the
requirements for the degree of
Bachelor of Science in Mechanical Engineering

Abstract

The Hyperloop is a ground-based transportation system proposed by Elon Musk in 2013 as a potential alternative to airplanes and high-speed rail. This thesis presents methods for first-order evaluation of design options for a Hyperloop system from technical and economic perspectives. The models are presented in generalized form so additional effects can be added by those with appropriate experience in the many different areas associated with long distance mass transport systems. The framework built in this thesis includes basic performance and cost analysis of the aerodynamics, levitation, propulsion, structure, and energy generation of a Hyperloop system. The first order models are intended to illustrate a process for investigating design trade-offs, but greater detail and domain specific expertise is needed to obtain realistic cost comparisons. The analysis culminates in a model to estimate the ticket cost for a Hyperloop route between any two cities, with many variables which can be input by the user to make conclusions about route feasibility.

Thesis Supervisor: Alexander H. Slocum
Title: Walter M. May and A. Hazel May Professor
of Mechanical Engineering

Contents

List of Figures

List of Tables

List of Variables

The following variables are general variables which define the geometry and other properties of the Hyperloop transport system. More specific variables are introduced in their respective sections.

N	number of passengers per pod (-)
t_p	time between pods (min)
v_{pod}	pod cruise speed (km/h)
m_{pod}	pod mass (kg)
L_{pod}	pod length (m)
a_p	maximum pod acceleration (g)
$c_{D,pod}$	pod drag coefficient (-)
A_{pod}	cross sectional area of pod (m^2)
A_{tube}	cross sectional area of tube (m^2)
A_{ratio}	ratio of pod to tube cross section ratio from Kantrowitz limit (-)
κ	percentage of area ratio up to Kantrowitz limit (-)
$D_{tube,i}$	inner diameter of tube (m)
t	tube thickness (mm)
$c_{D,tube}$	tube drag coefficient (-)
η	efficiency of linear induction motor (-)
γ	efficiency of vacuum pump (-)
P_a	air pressure inside tube (Pa)
ρ	air density inside tube (kg/m^3)
T_a	air temperature inside tube (K)
H	pylon height (m)
L	pylon span (m)
U	ambient wind speed (km/h)
ρ_{amb}	ambient air density at STP (kg/m^3)
S	design safety factor (-)
σ_y^T	tensile yield strength of concrete (MPa)
σ_y^C	compressive yield strength of concrete (MPa)
E	Young's Modulus of concrete (GPa)
a_{PG}	Peak ground acceleration during earthquake (g)
I	average annual solar irradiance in Southwestern US (kWh/m^2/day)
c_f	average number of sunny days per year in Southwestern US (-)
α	efficiency of solar panels (-)
λ	fraction of tube length allocated for solar panels (-)

Introduction

1.1 System Overview

The Hyperloop was first introduced in 2013 by SpaceX as an innovative mode of transportation that could compete with planes, trains, and cars in both speed and cost[1]. The underlying principle behind Hyperloop is relatively simple - any object moving through space at a given speed encounters resistance, so the ideal transportation system will minimize resistance. The dominant modes of resistance are aerodynamic drag and friction. Trains solve the friction problem by using magnetic levitation to eliminate contact between the train and the ground. Unfortunately, air resistance limits how fast the train can go even as trains are designed to be more aerodynamic. Airplanes solve both problems by flying tens of thousands of feet in the air where the air density is exponentially lower than the air density at sea level. However, planes have to expend massive amounts of energy throwing enough air down at the ground to keep the plane flying.

The approach Hyperloop takes to solve both problems is to recreate a low density environment at sea level. By moving an object through a sealed tube that has been pumped down to a thousandth of atmospheric pressure, the object can benefit from the near-zero drag at low air densities without having to expend energy going up tens of thousands of feet in the atmosphere to travel in that low air density environment. Friction can be eliminated by levitating the object either on a cushion of air or through magnetic repulsion. Propulsion is provided by linear induction motors powered by solar panels mounted above the tubes. With near-zero aerodynamic drag and minimal frictional losses, it may be possible to power the system entirely on solar energy. The concept is intended to serve high-traffic city pairs that are less than 900 miles apart.

1.2 Background

The concept of moving through a partially evacuated tube is not new. As early as 1909, rocket pioneer Robert Goddard suggested the idea of vacuum trains. In the early 2000s a national transportation project using magnetic levitation in vacuum trains, known as Swissmetro, began. The project later shut down due to questions about economic viability but was the first mass-scale attempt to bring such a technology to fruition.

The Hyperloop Alpha white paper combined many of these historical concepts and reignited interest in the concept and spurred a great deal of public interest in the concept. Two years after publishing the white paper, SpaceX announced the Hyperloop student competition in an attempt to catalyze open source development of the concept. Several companies were also founded soon after the white paper was published, most notably Virgin Hyperloop One and Hyperloop Transportation Technologies. However, public opinion of Hyperloop has fluctuated since the white paper was published as there is no consensus on the feasibility of the system.

Kantrowitz Limit

2.1 Overview

Any object moving through a tube (or any enclosure for that matter) encounters a fundamental limit on how fast it can go. This is because the airflow must speed up as it moves around the object in order to preserve mass conservation. However, once the airflow downstream the object reaches sonic speeds (Mach number of 1), the air can no longer speed up to go around the object and we say that the flow is choked. The object can no longer speed up as it is forced to move a mass of air accumulating in front of it. This fundamental limit on speed is known as the Kantrowitz Limit [5]. Once the limit is reached, the object will experience an exponential increase in air resistance as it behaves like a syringe and must move the entire column of air in the tube.

There are two solutions to overcome the Kantrowitz Limit. The first is to increase the cross-sectional area of the tube so that the air has more room to bypass the tube. Obviously this isn't ideal because the cost of the tube scales with the cross-sectional area. The other option is to actively remove the air accumulating in front of the pod. This may be possible by placing a pump at the front of the pod, as suggested in the Hyperloop Alpha white paper, but further research must be done to explore whether commercial pumps can operate at the necessary mass flow rates to prevent the column of air from forming. Furthermore, supersonic flow inside of a tube will lead to shock waves which present their own set of problems. To simplify this first-order analysis of the Hyperloop concept, we will assume that the pod operates within the Kantrowitz limit i.e. no pumps to actively suck in choked air at speeds past the Kantrowtiz limit.

2.1.1 Assumptions & Variables

The Kantrowitz Limit will gives us a maximum pod-to-tube area ratio for a given pod speed. To make use of the constraint, we must fix two of the following variables: pod speed, pod area, and tube area. To aid our analysis, we make the following assumptions

1. The pod travels at a cruise speed of 450 km/h. This speed will be verified once we have derived the governing relationship for the Kantrowitz Limit.
2. The cross-section area of the pod is fixed at 1.4 m^2, taken from the Hyperloop white paper.
3. While the Kantrowitz Limit presents a maximum pod-to-tube ratio, we will only design to a fraction, κ, of this maximum to account for space in the tubes for levitation, propulsion, and other components. For this analysis, κ is assumed to be 70%.

Table 2.1: Parameters used in Kantrowitz limit derivation

Variable	Description
$\dot{m}_0$	Mass flow rate upstream of pod
$\dot{m}_4$	Mass flow rate downstream of pod
M	Mach number
γ	Heat capacity ratio
A	Cross-section area
R	Universal gas constant
P_t	Stagnation pressure
T_t	Stagnation temperature

2.2 Derivation

It is useful to derive the Kantrowitz Limit because it gives the maximum ratio of pod to tube area at a given speed before the flow becomes choked. The following derivation is summarized from research done by Andrew Kantrowitz, who originally discovered the phenomenon in the 1940s [6]. The mass flow rates upstream and downstream of the pod are given from compressible flow theory

$$\dot{m}_0 = \sqrt{\frac{\gamma}{R}} M_0 \left(1 + \frac{\gamma - 1}{2} M_0^2\right)^{\frac{\gamma+1}{2(\gamma-1)}} \frac{P_{t0} A_0}{\sqrt{T_{t0}}} \tag{2.1}$$

$$\dot{m}_4 = \sqrt{\frac{\gamma}{R}} M_4 \left(1 + \frac{\gamma - 1}{2} M_4^2\right)^{\frac{\gamma+1}{2(\gamma-1)}} \frac{P_{t4} A_4}{\sqrt{T_{t4}}} \tag{2.2}$$

Conservation of mass requires that these two mass flow rates be equal. The Kantrowitz Limit can then be derived by setting $M_4 = 1$, as this is the point where the flow becomes choked. Solving for the area ratio gives the following expression

$$\frac{A_{bypass}}{A_{tube}} = \left[\frac{\gamma - 1}{\gamma + 1}\right]^{\frac{1}{2}} \cdot \left[\frac{2\gamma}{\gamma + 1}\right]^{\frac{1}{\gamma-1}} \cdot \left[1 + \frac{2}{\gamma - 1}\frac{1}{M^2}\right]^{\frac{1}{2}} \cdot \left[1 - \frac{\gamma - 1}{2\gamma}\frac{1}{M^2}\right]^{\frac{1}{\gamma-1}} \tag{2.3}$$

Here A_{bypass} is the area between the pod and the tube and M is the Mach number upstream of the pod. The equation tells us the maximum ratio of the bypass cross section area to the tube cross section area before the flow becomes choked.

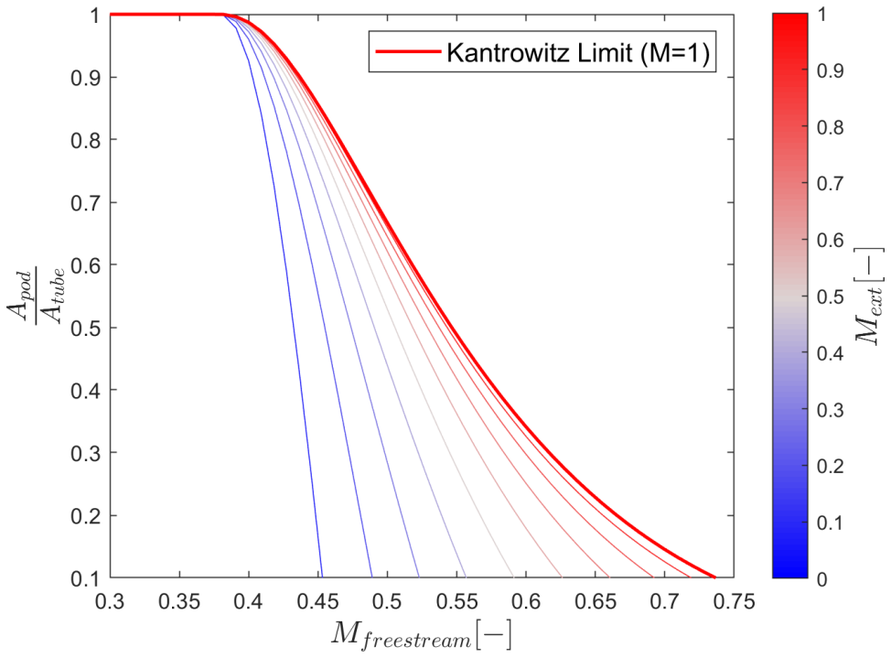

Figure 2-1: Area ratio as function of free-stream mach number. M_{ext} is the Mach number of the flow around the pod.

Fig. 2-1 shows how the external Mach number changes as we vary the area ratio and Mach number upstream of the pod. For a given freestream Mach number, there is a limit on how large the pod-to-tube area ratio can go before we hit the Kantrowitz Limit. To minimize costs, we would like to operate as close to the Kantrowitz Limit as possible since this gives the smallest possible tube cross-section, thus minimizing costs. We've chosen a speed of V_{pod} =724 km/h (450 mph) which translates to a Mach number of $M = 0.58$. Inspection of the red curve in Fig. 2-1 reveals that a Mach number of 0.58 is sufficiently close to the inflection point - where the tradeoff between going faster at the cost of lower area ratios is near optimal. Thus, we have verified assumption 1 and will maintain a pod speed of 724 km/h through the remainder of the Hyperloop analysis. At the specified pod speed, the best area ratio we can get is 0.39. Taking the pod cross section from assumption 2 and going up to 70% of the limit, as specified by the parameter κ in assumption 3, gives a tube cross sectional area of 5.11 m^2 which results in a tube inner diameter $D_{tube,i}$ of 2.55 m.

Pod

3.1 Overview

According to the Hyperloop Alpha white paper, each pod is designed to carry 28 passengers. Passengers are seated in a reclined manner to minimize pod cross-section. The paper also reports a number of variables defining the geometry and mass of the pod. To simplify our analysis, we will use the geometric and mass variables presented in the Hyperloop white paper.

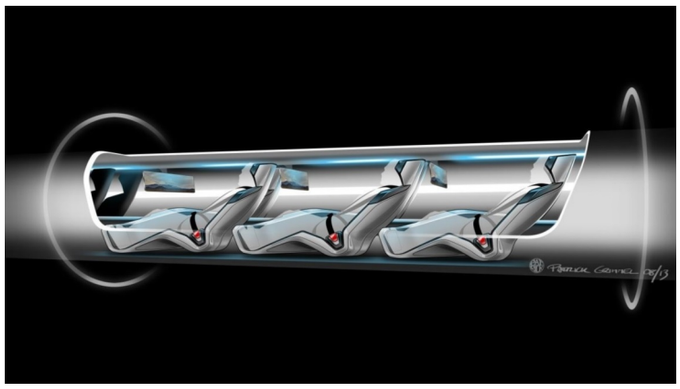

Figure 3-1: Artist rendition of Hyperloop pod [1].

3.1.1 Assumptions & Variables

We will need to make a few assumptions about the geometry and mass characteristics of the pod.

1. Passengers are seated approximately 6 ft apart
2. The pod length will be scaled by a factor of $\epsilon = 1.5$ to account for propulsion, levitation, and other components

Table 3.1: Pod variables reported in Hyperloop white paper

Variable	Value	Description
w	1.35	width (m)
h	1.1	height (m)
A	1.4	cross-section area (m^2)
ϵ	1.5	pod length scale factor (-)
N	28	number of passengers per pod (-)
m_p	2800	mass of all passengers in pod (kg)
m_s	3100	structural mass of pod (kg)
m_i	2500	interior mass of pod (kg)
m_{LIM}	700	mass of linear induction motor (kg)
m_l	1000	mass of levitation components (kg)

3.2 Geometry

We will need to estimate the length of the pod for our propulsion analysis in the later sections. The length is not given in the white paper so we will approximate it. Let dl represent the spacing between passengers and η represent a length scale factor for non-passenger components in the pod. The length of the pod can be calculated as follows

$$L = N \cdot dl \cdot \epsilon = 76.44m \tag{3.1}$$

3.3 Risk Factors

1. The pod cross-section area proposed in the Hyperloop white paper leads to an extremely cramped design. While this is cost effective, passenger studies may reveal that it is too uncomfortable to be practical. The models presented in this thesis can help designers rapidly iterate different pod cross-section areas in order to investigate the tradeoff between cost efficiency and passenger comfort.

Levitation

4.1 Overview

The following sections compare three different approaches to support the Hyperloop pod - air bearings, passive magnetic levitation, and active magnetic levitation. In the original white paper, air bearings were suggested to levitate the pods on a cushion of air. However, the primary concern with air bearings is whether the pod can carry the necessary volume of air to maintain levitation through the duration of the trip. Analysis will be done here to thoroughly compare the feasibility and design trade-offs of each solution.

4.2 Air Bearings

Air bearings are devices that utilize a thin film of pressurized gas to create a low friction interface between surfaces. There are two classes of air bearings: aerostatic and aerodynamic. Aerostatic bearings feed externally-pressurized gas through an opening in the bearing, similar to an air hockey table. Aerodynamic bearings leverage the relative velocity between the bearing and ground to pressurize the gas. In the case of Hyperloop the pod is moving and thus the bearing is aerodynamic. We will use the term "air bearing" in this section to mean "aerodynamic bearing". For our analysis, the air bearing moves at a speed U and has a rectangular shape, as shown in Fig. 4-1.

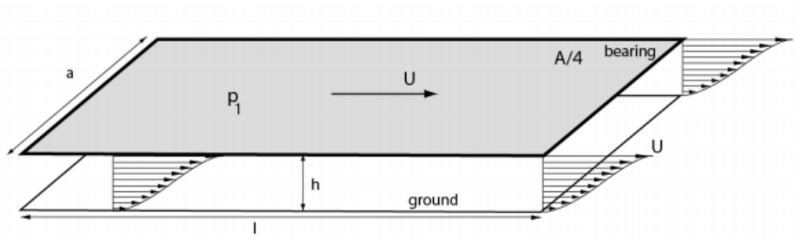

Figure 4-1: A rectangular air bearing moving at constant speed U [2].

4.2.1 Assumptions & Variables

To simplify our analysis, we make the following assumptions

1. The air bearing is rectangular, with a length of l and width of a, and moves at speed U
2. The gap height, h, is much smaller than the dimensions of the air bearing
3. The airflow trapped underneath the air bearing is characteristic of Couette Flow
4. The pressure field underneath the pod has a linear gradient
5. The flow underneath the air bearing is incompressible

Table 4.1: Variables used in air bearing analysis

Variable	Value	Description
a	0.5	Width of air bearing (m)
l	0.1 - 2	Length of air bearing (m)
U	450	air bearing speed (mph)
ρ	1.225	Air density in flow underneath air bearing (kg/m^3)
μ	1.81 $\cdot 10^-5$	Air viscosity in flow underneath air bearing (Pa-s)
m_{pod}	10100	Total pod mass (kg)

4.2.2 Derivation

Because the thickness of the air underneath the air bearing is usually several orders of magnitude less than the dimensions of the air bearing itself, lubrication theory is a good approximation to this flow scenario. Under lubrication theory, the Navier-Stokes equations simplify to:

$$\frac{\partial P}{\partial y} = 0 \tag{4.1}$$

$$\frac{\partial P}{\partial x} = \mu \frac{\partial^2 u}{\partial y^2} \tag{4.2}$$

where u is the velocity profile between the air bearing and ground, μ is the kinematic viscosity, and $\frac{\partial P}{\partial x}$ is the pressure gradient along the flow direction. Double integration of Equation 4.2 and application of boundary equations gives us the velocity profile of a classic Couette-flow.

$$u(y) = \frac{1}{2\mu} \frac{\partial P}{\partial x} \cdot y(y - h) \tag{4.3}$$

Here h is the gap between the air bearing and the ground. Integrating the velocity profile along the gap and along the width of the bearing gives the volumetric flow rate, $\dot{Q}$.

$$\dot{Q} = \int_0^a \int_0^h u(y)\, dy\, dz = \frac{h^3 a}{12\mu} \frac{\partial P}{\partial x} + U \cdot \frac{ha}{2} \tag{4.4}$$

Assuming the flow is incompressible (constant density everywhere), we can calculate the mass flow rate $\dot{m}$ necessary to maintain an air bearing at a gap height h.

$$\dot{m} = \rho \dot{Q} = \frac{\rho h^3 a}{12\mu} \frac{\partial P}{\partial x} + U \cdot \frac{\rho h a}{2} \tag{4.5}$$

Integrating the pressure gradient along the length of the air bearing gives the following expression.

$$\dot{m} = \frac{\Delta P \rho h^3 a}{12\mu l} + U \cdot \frac{\rho h a}{2l} \tag{4.6}$$

Table 4.2: Effect of design parameters on mass flow rate

Design Parameter	**Effect on $\dot{m}$**	**Description**
ΔP	Linear increase	Pressure difference across air bearing
h	Cubic increase	Air bearing gap height
a	Linear increase	Air bearing width
l	Linear decrease	Air bearing length
U	Linear increase	Pod speed

The air bearing gap height is found to be the driving parameter for the system since the required mass flow rate scales with the cube of the gap height but only linearly with other design parameters. The pod speed U is not a parameter that we can vary freely as it is set by the Kantrowitz Limit. The width w of the air bearing is limited by the width of the pod and the pressure difference has to satisfy $m_{pod} = P_{avg} \cdot A_{bearing}$, where $m_{pod}g$ is the weight of the pod and P_{avg} is the average pressure in the area underneath the air bearing. To simplify our analysis, we will assume that the pressure at the the end of the air bearing is equal to the ambient air pressure in the tube and that the pressure distribution within the air bearing is linear. The average air pressure can then be written as:

$$P_{avg} = \frac{1}{l} \int_0^l P(x)\, dx = P_2 + \frac{\Delta P}{2} \tag{4.7}$$

where P_2 is the pressure at the end of the air bearing. For a given air bearing area, there is a minimum average pressure within the air bearing that must be maintained so that the lift force from the air bearings is equal to the weight of the pod. We can see that there is a direct relationship between the air bearing area and pressure difference across the air bearing in the constraint:

$$m_{pod}g = P_{avg} \cdot A_{bearing} = \left(P_2 + \frac{\Delta P}{2} \right) A_{bearing} \tag{4.8}$$

Because the air bearing area determines the pressure difference necessary to lift the pod, the only design parameters we can manipulate in Equation 4.6 is the air bearing gap height and the air bearing length. If we fix the width w of the air bearing, varying the length of the air bearing is equivalent to varying the area of the air bearing. We can then investigate how the mass flow rate changes as a function of the gap height and the air bearing area.

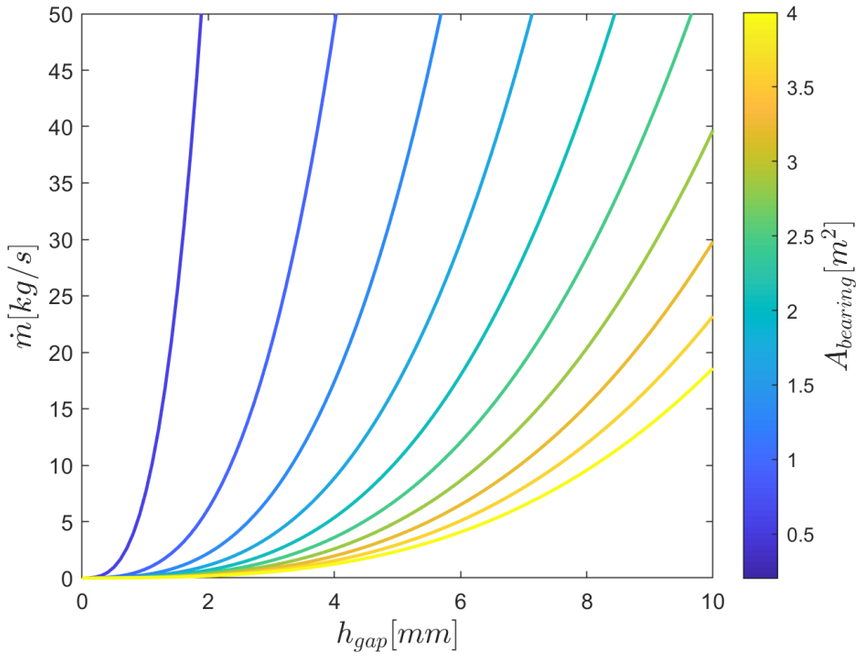

Figure 4-2: Air bearing flow rate as a function of gap height and air bearing area.

4.2.3 Risk Factors

Using the set of curves in Fig. 4-2 we can easily come up with some numerical examples. For instance, if the gap height is 5mm, the smallest mass flow rate we can have while maintaining levitation is roughly 2.4 kg/s. This requires an air bearing area of 4 m^2. Given that the pod is designed to move at a cruise speed of 450 mph, we can see immediately that the mass flow rate necessary for air bearing levitation is unfeasible for potential Hyperloop routes. For example, the distance between Los Angeles and San Francisco is 382 miles bringing our route duration to 3056 seconds. Thus, the pod would need to be equipped with 7334 kg of air. Assuming the air is stored at atmospheric pressure, it would take 5986 m^3 of space to store enough air on the pod for the LA to SF journey. Clearly, this is unfeasible. Even if we compressed the air to 6000 psi, which is on the upper bound of what commercial air tanks can reliably achieve, the volume of air needed would still be 15 m^3. While this is certainly a far more manageable volume to store, the energy cost of compressing that volume of air for every trip would be immense and unfeasible at scale. The final option is to reduce the gap height between the air bearing and the ground in an attempt to reduce the required mass flow rate. However, there is a safety concern with an arbitrarily small gap height as any vibration could bring the pod into contact with the tube surface and lead to rapid deterioration of the pod at high speeds. Furthermore, there is a lower bound on the gap height as tolerances in manufacturing will limit how flat the interface between connecting tube segments can be. For these reasons, we conclude that air bearings are an unfeasible solution.

4.3 Magnetic Levitation

There are two types of magnetic levitation - active and passive. Active magnetic levitation takes advantage of the fact that the opposite poles of two separate magnets will repel each other. Using an electromagnet, the strength of the magnetic field as well as its polarity can easily be varied by modulating the current flowing through the electromagnet. By placing electromagnets along the tube and in the pod, levitation can be achieved by modulating the current in the electromagnets such that the magnetic fields repel each other and lift the pod up to the desired height. However, because the magnetic field strength varies inversely with the square of the distance, any minor deviation from the desired gap height will lead to instabilities. The inherent instability of active maglev can be cancelled with fine feedback control but the constant adjustment may induce vibrations in the system.

Much of the work on passive maglev was done in the 1990s by Dr. Richard Post at the Lawrence Livermore National Laboratory [7]. Dr. Post developed the idea of Inductrack - a passive, fail-safe electrodynamic levitation system. The underlying concept takes advantage of various physical phenomena derived from Maxwell's equations, but in essence the motion of a set of permanent magnets over a conductive sheet induces currents in the track. These induced currents then generate their own magnetic fields which repel the magnetic fields produced by the permanent magnets and subsequently create lift. Passive maglev presents the following advantages over active maglev:

1. Simpler implementation - no need for advanced feedback control systems
2. Improved stability - deviations from the designed gap height create strong restoring forces
3. Source of levitation is propulsion itself - no additional source of power needed to generate lift
4. Lower costs - conductive track far cheaper than a row of electromagnets hundreds of km long
5. Safer - in the event of power loss, the pod gently glides down to the ground whereas with active maglev the pod will suddenly slam back to the ground

4.3.1 Assumptions & Variables

For this analysis, we will assume passive maglev is the source of levitation given the many advantages over active maglev listed above. The list of assumptions are as follows

1. The magnetic levitation system is passive
2. A Halbach array is used to enhance the magnetic field
3. The conductive track is a plate of aluminum, with a resistivity of $2.65 \cdot 10^{-}8\ \Omega - m$ and permeability of $1.26 \cdot 10^{-}6\ H/m$

4.3.2 Derivation

The following derivation is a summary from models of passive magnetic levitation that were developed and investigated by Dr. Richard Post at the Lawrence Livermore National Laboratory[7]. Specifically, the derivation is for an arrangement of permanent magnets - the Halbach Array - moving over a conductive plate. The Halbach Array is a special arrangement of magnets which leads to cancellation of the magnetic field on one side and augmenting of the magnetic field on the other side. This is ideal for a maglev application because all of the magnetic field strength is concentrated between the magnet and conductor and cancels out on the other side. Fig 4.3 shows a diagram of a Halbach Array. Each cube represents a permanent magnet, with the arrow indicating the direction of the magnetic field. The field below the array would nearly double in strength while the field above the array would cancel out.

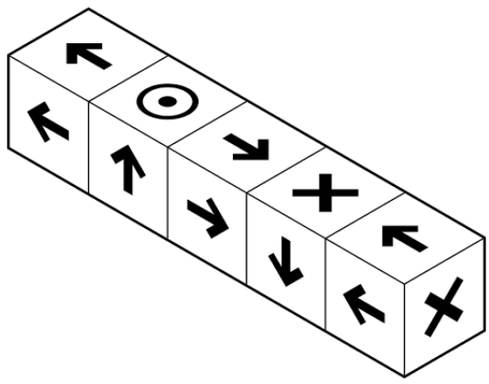

Figure 4-3: Halbach Array [3].

The strong magnetic field created by the Halbach Array can be expressed as

$$B_x(t) = B_0 \sin(kx) e^{-k\Delta z} \tag{4.9}$$

$$B_z(t) = B_0 \cos(kx) e^{-k\Delta z} \tag{4.10}$$

where B_x is the component of the magnetic field in the direction of motion, B_z is the component of the magnetic field normal to the direction of motion, B_0 is the peak strength of the magnetic field at the surface of the Halbach array, k is the wavenumber of the periodic Halbach array, x is the distance traveled by the Halbach array in the direction of motion, and Δz is the gap height between the Halbach array and the conductor. It should be noted that the Halbach array is periodic so we can write the wavenumber in terms of the wavelength, λ, of the Halbach array

$$k = \frac{2\pi}{\lambda} \tag{4.11}$$

As the array of permanent magnets moves alongside the conducting track at the pod velocity U, the relative motion will create a a change in magnetic flux, ϕ_B, due to the magnetic field vector B_x moving through the cross-section of the conductive track. Here we will model the conductor as a rectangular cross-section with width w_c and thickness t_c. Lenz's Law shows that a voltage, V, will be induced in the conductor which is proportional to the change in magnetic flux and in a direction which opposes the change that produced it.

$$V = I_e R_c + I_e \frac{\partial L_c}{\partial t} = -\frac{\partial \phi_B}{\partial t} \tag{4.12}$$

Here we have modified Ohm's law by modeling the conductor as both a resistor and an inductor. I_e is the induced eddy current in the conductor, R_c is the resistance of the conductor, and L_c is the inductance of the conductor. The force vector that arises from the interaction between the Halbach magnetic field and the current induced in the conductor can be expressed by the Lorentz force

$$F_z = I_e w_c \times B_x \tag{4.13}$$

$$F_x = I_e w_c \times B_z \tag{4.14}$$

Solving for the induced current in Equation 4.12 and substituting into equations 4.13 and 4.14 gives the following expressions for the lift and drag force

$$F_{lift} = \frac{B_0^2 w_c^2}{2kL_c} \cdot e^{-2k\Delta z} / \left[1 + \left(\frac{R_c}{\omega L_c}\right)^2\right] \tag{4.15}$$

$$F_{drag} = \frac{B_0^2 w_c^2}{2kL_c} \cdot \frac{R_c}{\omega L_c} \cdot e^{-2k\Delta z} / \left[1 + \left(\frac{R_c}{\omega L_c}\right)^2\right] \tag{4.16}$$

where ω is the frequency of the magnetic flux and can be written as $\omega = kU$. The lift to drag ratio can now be calculated directly with Equations 4.15 and 4.16.

$$\frac{F_{lift}}{F_{drag}} = \frac{\omega L_c}{R_c} \tag{4.17}$$

Interestingly, the lift to drag ratio actually increases monotonically with speed, unlike the aerodynamic lift to drag ratio which increases then decreases with speed. However, the lift to drag ratio written in Equation 4.17 is incomplete. The density of eddy currents induced in the conductor is usually highest near the surface and decreases towards the center. The region where most of the eddy currents accumulate is known as the skin depth. This has the effect of increasing the resistance of the conductor because the effective cross-section area is reduced. The lift to drag ratio after factoring in the skin effect is written as

$$\frac{L}{D} = \frac{1}{k\delta}\left(\sqrt{1 + \frac{k^4\delta^4}{4}} - \frac{k^2\delta^2}{2}\right)^{\frac{1}{2}} \tag{4.18}$$

where the skin depth, δ, is given by

$$\delta = \sqrt{\frac{2\rho}{\omega \mu_o}} \tag{4.19}$$

We can see that the modified lift to drag ratio is a function of the pod speed U and the wavelength k of the periodic Halbach array in Figure 4-4.

As shown in Fig. 4-4, the lift to drag ratio increases monotonically with the array wavelength and pod speed. Because the pod speed is constrained by the Kantrowitz Limit, it would seem that any lift to drag ratio can be achieved by arbitrarily increasing the Halbach array wavelength. However, it is important to note that the cost of the maglev system scales with the wavelength of the array and the lift generated by the array scales proportionally with the wavelength. The optimization problem is then to find the minimum wavelength necessary to produce sufficient lift to levitate the pod at a given height. We deemed this optimization problem unnecessary to solve given the goal of the study is to quickly determine the feasibility of the Hyperloop concept. Therefore, we fixed the Halbach wavelength, λ, to 0.5m which gives a conservative lift to drag ratio of 19.5.

At this lift to drag ratio, the magnetic drag force on the pod is given by

$$F_{drag} = \left(\frac{L}{D}\right)^{-1} \cdot m_{pod} g = 5.09kN \tag{4.20}$$

$$E_{drag} = F_{drag} * d_{km} = 5.09 MJ/km \tag{4.21}$$

where m_{pod} is the mass of the pod, d_{km} is the distance over which the drag force acts, and E_{drag} is the energy needed per kilometer to overcome magnetic drag.

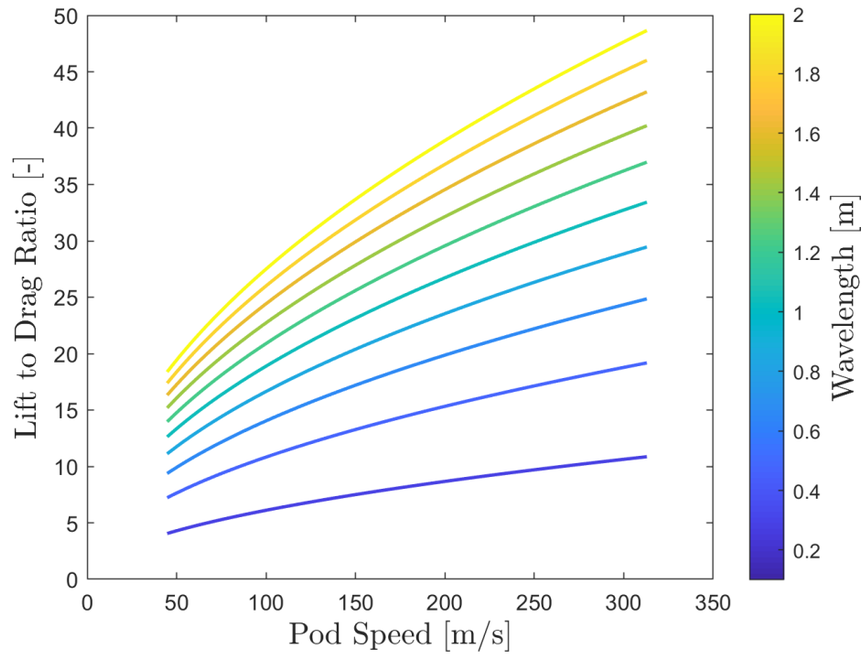

Figure 4-4: Magnetic lift to drag ratio as a function of pod speed and Halbach array wavelength

4.3.3 Sizing

We will now calculate the size of the conductive track and Halbach array needed to generate the necessary lift to levitate the pod at a given gap height. The following expressions are summarized from the research done by Dr. Richard F. Post [7]

$$\frac{F_L^{max}}{A} = \frac{B_0^2}{\mu_0} \cdot e^{(-2k\Delta z - k\Delta c)} \tag{4.22}$$

where F_L^{max} is the maximum lift force when $V_{pod} \to \infty$, A is the area of the Halbach array, B_0 is the peak strength of the magnetic field, μ_0 is the permeability of free space, k is the wavenumber of the Halbach array, δz is the levitation gap height, and Δc is the thickness of the conductor. The lift force is then given by

$$F_L = F_L^{max} \cdot \frac{\alpha}{\beta} \tag{4.23}$$

$$\alpha = \left(\sqrt{1 + \frac{k^4\delta^4}{4}} - \frac{k^2\delta^2}{2} \right)^{\frac{3}{2}} \tag{4.24}$$

$$\beta = k\delta + \left(\sqrt{1 + \frac{k^4\delta^4}{4}} - \frac{k^2\delta^2}{2} \right)^{\frac{3}{2}} \tag{4.25}$$

Combining Equations 4.22-4.25, we can write the magnetic lift force in functional form

$$F_L = f(B_0, \mu_0, A, k, \Delta z, \Delta c, \delta) \tag{4.26}$$

To quickly generate numerical examples, we will hold most of the parameters in Equation 4.26 constant while varying the area, A, of the Halbach array and the thickness, Δc, of the conductor. The variables are written in Table 4.3, where we have made the following assumptions

1. The wavelength, λ, of the Halbach array is 0.5. The wavenumber of the Halbach array is then given by Equation 4.11
2. The thickness, d_h, of the Halbach array is $\frac{\lambda}{4} = 0.125m$
3. The levitation gap height, Δz, is 76.2mm (3 inches). This is a typical levitation height done on commercial maglev trains.

Table 4.3: Parameters in magnetic lift equation

Free Parameter	Fixed Parameter
Δc	$\mu_0 = 4\pi \cdot 10^{-}7$ H/m
A	$k = 12.5m^{-1}$
	$\Delta z = 76.2 * 10^{-3}$ m
	$\delta = 4.09 * 10^{-3}$ m
	$B_0 = 0.9$ T

4. The peak strength of the magnetic field, B_0, is 0.9 Tesla. This is typical for commercial NdFeB (Neodymium-Iron-Boron) magnets.

5. The skin depth, δ, is 4.09mm. This is given by Equation 4.19.

We can now visualize how the magnetic lift force varies as a function of the area, A, of the Halbach array and the thickness, Δc, of the conductive track. For a Halbach array area of $0.01m^2 \leq A \leq 2m^2$ and conductive track thickness of $0.0064m$ (0.25in) $\leq \Delta c \leq 0.0254m$ (1 in), the following relationship results

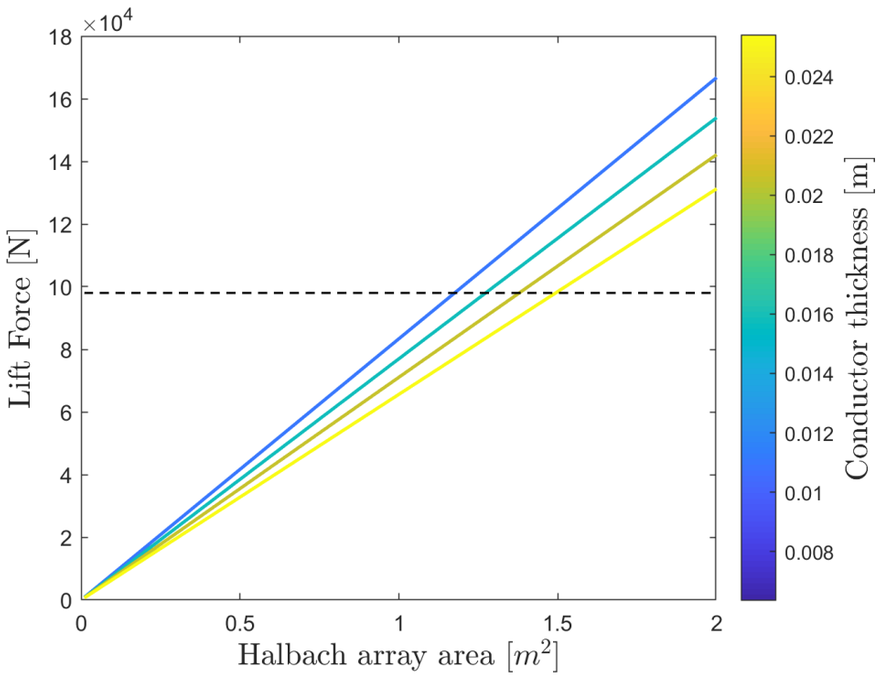

Figure 4-5: Magnetic lift force as a function of Halbach array area and conductor thickness

Fig 4-5 shows that there is a linear relationship between the magnetic lift force and the Halbach array area. Additionally, at a fixed Halbach area the lift force decreases as the conductor thickness increases. The dashed black line is the lift force needed to levitate a pod of weight $m_{pod}g$, where $m_{pod} = 10,000$kg is the pod mass. If we inspect the dark blue line, which is at a conductor thickness of $0.0064m$ (0.25in), we can see that at a Halbach area of 1 m^2 the passive maglev system is capable of lifting about 8,000 kg per square meter to a levitation gap of $76.2mm$ (3 in). To estimate cost, we will proceed with the intersection of the dashed black line with the curve at a conductor thickness of $0.0064m$ (0.25in) as our design point.At this point, the Halbach array has an area of 1.2 m^2.

We can now calculate the cost of the passive maglev system. The variables used in our cost estimation are listed in Table 4.4

Table 4.4: Parameters in maglev cost estimation

Variable	Value	Description
ρ_n	7010	Density of Neodymium (kg/m^3)
C_n	41.7	Cost per kg of Neodymium ($/kg)
ρ_a	2710	Density of Aluminum (kg/m^3)
C_a	1.48	Cost per kg of Aluminum ($/kg)

The area of the Halbach array is expressed as

$$A = \lambda \cdot w_h \tag{4.27}$$

where λ is the wavelength of the Halbach array and w_h is the width of the Halbach array. At our design point (A=1.2m^2), the width, w_h, is 2.4m. Given the magnet thickness, d_h, from assumption 2 the volume and cost of the Halbach array are given by

$$V_h = A \cdot d_h = 0.15m^3 \tag{4.28}$$

$$C_h = V_h \cdot \rho_n \cdot C_n = \$43,800 \tag{4.29}$$

We will assume that the width of the conductive track, w_c, is equal to the width, w_h, of the Halbach array. The volume and cost of the conductive track, per km of route, are given by

$$V_c = w_c \cdot \Delta c \cdot 1000m = 15.36m^3/km \tag{4.30}$$

$$C_c = V_c \cdot \rho_a \cdot C_a = \$61,600/km \tag{4.31}$$

4.3.4 Stability

One of the fundamental drawbacks with passive maglev is that it is under-damped to oscillations about the vertical axis (yaw rotation) and translation about the horizontal axis. Thus the system is only stable in four out of the six degrees of freedom - horizontal translation and yaw rotation are under-damped. Research of the literature reveals several methods to overcome this drawback and stabilize the system in all 6 degrees of freedoms. One of the primary methods is the use of stabilizing coils (or any conductor) to provide a restoring force to lateral displacements in the underdamped degrees of freedom [8].

In the theme of first-order analysis, we present a simple model of a stabilization mechanism. Two conductive plates are placed symmetrically on either side of the tube. Two Halbach arrays, each one oriented with the strong-side of the magnetic field pointed towards the conductive plate, are placed symmetrically inside of the Hyperloop pod. Any lateral displacement will induce currents in the two conductive plates, thus generating a restoring force which brings the pod back to equilibrium. At the equilibrium position, there is little to no lateral force on the pod as the two magnetic fields generated by the stabilizing Halbach arrays are symmetric and cancel out. While this is an extremely simplistic model which needs iteration to determine the stiffness, damping ratio, and restoring forces generated by a stabilizing design, it is sufficient for cost estimation.

We will assume that the two stabilizing conductive plates and Halbach arrays have the same dimensions as the conductive track and Halbach array we sized in the previous section. Then, the total cost of the passive maglev system with stabilization is

$$C_h = 3 \cdot V_h \cdot \rho_n \cdot C_n = \$131,400 \tag{4.32}$$

$$C_c = 3 \cdot V_c \cdot \rho_a \cdot C_a = \$184,800/km \tag{4.33}$$

where we have taken Equations 4.29, 4.31 and multiplied by a factor of 3 to take into account the two additional stabilizing conductive plates and Halbach arrays.

4.3.5 Risk Factors

1. The conductive track presented here is can be optimized to improve the lift to drag ratio. The Inductrack concept, developed by Dr. Post at the Lawrence Livermore National Laboratory, suggests the use of Litz cables for the conductive track. Litz cables reduce the eddy current losses caused by the skin depth effect. The models presented in the Inductrack paper show that a lift to drag ratio of 280 can be achieved at speeds of 500 km/h [7]. The lift to drag ratio achieved with Litz cables is a full order of magnitude higher than the lift to drag

ratio achieved with a simple aluminum plate conductor. Further analysis should investigate the tradeoff between lower magnetic drag but higher costs with Litz cables comprising the conductive track.

2. Static levitation is not possible with passive maglev - relative motion is needed to generate lift. The pod will then need to be equipped with wheels, similar to the landing gear on airplanes, to support its weight until it reaches the minimum speed necessary to lift itself. Minimum speed is usually on the order of 30-40 km/h, which is only a fraction of the cruise speed [7]. Nonetheless, the energy cost per km of passive maglev will increase when accounting for the friction between the pod and track during the acceleration/deceleration phase.

3. The stabilization design presented here is extremely simplistic and needs thorough iteration to determine the specific geometry needed to meet stiffness, damping, and restoring force requirements. The cost metric presented for the stabilization system here is likely to be an upper bound, however, as the design presented in [8] suggests the use of stabilizing coils rather than a solid conductor which will drive material costs down.

Propulsion

5.1 Overview

Because levitation is essential to minimizing energy losses, any propulsion method has to be contactless. The Hyperloop Alpha white paper suggests using a linear induction motor (LIM) to propel the pod to cruise speed. Linear induction motors are analogous to rotary induction motors that have been "unrolled" to create linear motion instead of rotary motion. The stator is a set of electromagnets and the rotor is simply a conductive material such as aluminum. Propulsion is achieved by modulating current on the stator side to create a magnetic wave that travels along the length of the stator. The relative motion between this traveling magnetic wave and the rotor induces an electric current in the rotor. The induced current interacts with the magnetic wave to produce a linear force. The force and thus the acceleration of the pod can be controlled by varying the frequency input to the electromagnets which comprise the stator. Figure 5-1 illustrates the components of a linear induction motor - the stator is a repeating pattern of electromagnets and the rotor is a conductive bar.

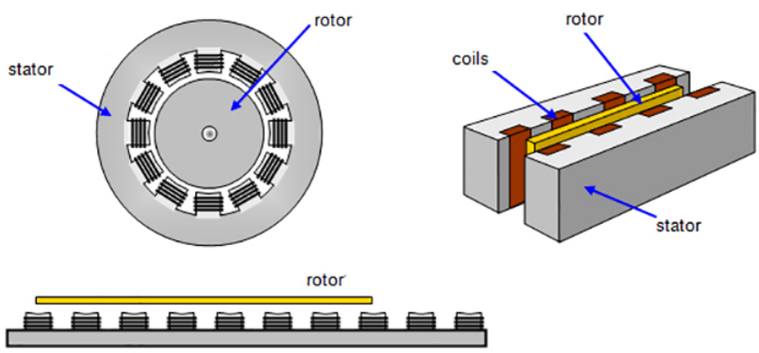

Figure 5-1: Components of a linear induction motor.

5.1.1 Propulsion & Levitation Coupling

It is important to note that the levitation and propulsion systems are inherently linked. The pod is equipped with a set of permanent magnets arranged into a Halbach array. The track has two separate elements - electromagnets and a solid conductor. The electromagnets generate the varying magnetic field which accelerate the pod forward, generating thrust. Then, the relative motion between the Halbach array on the pod and the solid conductor on the track creates a lift force which levitates the pod at a specified gap height, as discussed in the Section 4.

One of the key advantages of passive maglev is that levitation happens automatically once the linear induction motor propels the pod forwards. The relative motion between the Halbach array inside of the pod and the conductive track creates lift. In a sense, the linear induction motor is doing "double duty" by creating both lift and thrust.

5.1.2 Assumptions & Variables

To simplify our analysis, we will use the cost metric for the linear induction motor design presented in the Hyperloop white paper rather than deriving the governing equations and computing a cost metric. Because the cost of placing electromagnets along the entire length of a route is prohibitively high, we will use a periodic acceleration design to save costs.

1. The cost per kilometer of LIM is $35 million, as calculated in the Hyperloop white paper
2. The minimum speed of the pod, v_{min}, is 90% the cruise speed of the pod, v_{pod} (450 mph)
3. The LIM accelerates the pod at 1g

5.2 Cost Estimation

The linear induction motor designed in the Hyperloop Alpha white paper provides an average propulsive power of 37 MW and a peak power of 56 MW (See A-4). The cost of the propulsion

Table 5.1: Variables used in linear induction motor design

Variable	Value	Description
C_{LIM}	35,000,000	Cost per kilometer of LIM ($)
v_{min}	405	Minimum allowable pod speed (mph)
a_d	-0.5	Deceleration from drag (g)
a_p	1	Acceleration from LIM (g)
η	0.8	Efficiency of LIM (-)

system is $35 million per km and this includes the cost of the stator, power electronics, and energy storage components. In assumption 1 we stated that the cost metric of $35 million per km is a reasonable metric. To test the validity of this assumption, we will derive the power consumption of our Hyperloop pod as it accelerates from rest to a cruise speed of v_{pod} =724 km/h (450m mph) at an acceleration of a_p =1g. Kinematic relations give

$$v_f = v_0 + a_p t \tag{5.1}$$

$$d = \frac{1}{2} a_p t^2 \tag{5.2}$$

$$P = \frac{1}{\eta} \frac{Fd}{t} = \frac{1}{\eta} \cdot \frac{m_{pod} \cdot a_p \cdot d}{t} \tag{5.3}$$

Equation 5.1 can be used to solve for the time t it takes for the pod to accelerate from $v_0 = 0$ to $v_f = v_{pod}$ at an acceleration of a_p. The time to accelerate, t, can be substituted into Equation 5.2 to solve for the distance, d, the pod travels during acceleration. Finally, the propulsive power needed for acceleration can be calculated using Equation 5.3, where η is the efficiency of the linear induction motor and m_{pod} is the mass of the pod. Solving the three equations results in a propulsive power of $P = 12.25W$. This calculation verifies that at a pod mass of $m_{pod} = 10,000kg$, as calculated in Section 3, the linear induction motor designed in the Hyperloop Alpha white paper provides the necessary propulsive power. Thus, we will proceed in the analysis with assumption 1. It is useful to note that above a pod mass of 30,000kg, the average power needed to accelerate the pod is greater than the average propulsive power provided by the linear induction motor specified in the Hyperloop Alpha white paper. Thus, assumption 1 will no longer hold true for a pod mass above 30,000kg. In this scenario, the designer should explore linear induction motor designs that will meet the power requirements and derive cost metrics for said design.

5.3 Periodic Acceleration

This cost of the LIM is driven by the sheer volume of electromagnets that need to be placed along the tube to propel the pod. It becomes apparent right away that this cost is prohibitively large for any route more than a few kilometers long. For example, one of the busiest corridors in the United States is between Los Angeles and San Francisco. The two cities are separated by 382 miles or 615 km. To propel a Hyperloop pod along this route would cost about $21.5 billion for just the propulsion components.

One possible solution is to place the linear induction motor periodically along the route instead of along the entire route. The pod will decelerate once there is no propulsive force to balance the forces of magnetic and aerodynamic drag. The problem is then to choose a spacing between adjacent LIM stators' that minimizes the cost per kilometer of the LIM while keeping the pod above a minimum allowable speed. The deceleration from drag, a_d, is calculated by dividing the total drag force by the mass of the pod and the minimum allowable speed, v_{min}, is simply 90% of the cruise speed. When there is no propulsive power (no LIM), the pod will decelerate. We calculate the time to reach the minimum speed and the distance the pod travels while decelerating from kinematics

$$t_{min} = \frac{v_{min} - v_{cruise}}{a_d \cdot g} = 39.84s \tag{5.4}$$

$$d = \frac{1}{2} a_d \cdot g \cdot t_{min}^2 = 0.4km \tag{5.5}$$

We now have the distance d between consecutive LIM components. Now, we determine the length of the LIM needed to bring the pod back up to cruise speed in the same manner

$$t_{LIM} = \frac{v_{cruise} - v_{min}}{a_p \cdot g} = 2.05s \tag{5.6}$$

$$d_{LIM} = \frac{1}{2} a_p \cdot g \cdot t_{LIM}^2 = 0.02km \tag{5.7}$$

We now define the cycle distance as the distance the pod travels to decelerate down to the minimum allowable speed and then accelerate back to cruise speed. Then this cycle distance can be used to calculate the length of LIM components needed per km of route.

$$d_{cycle} = d + d_{LIM} = 0.42km \tag{5.8}$$

$$L_{LIM} = \frac{d_{LIM}}{d_{cycle}} = 0.05km \tag{5.9}$$

The cost from assumption 1 is now modified to reflect this periodic acceleration design

$$C_{periodic} = C_{LIM} \cdot L_{LIM} = 1,700,000 \frac{\$}{km} \tag{5.10}$$

This design reduces the original cost of the linear induction motor by a factor of 20. The cost of the propulsion components for the route connecting Los Angeles and San Francisco is now roughly $1 billion.

5.4 Risk Factors

1. Passengers may find it annoying or nauseating to periodically accelerate back to cruise speed at 1g over the entire duration of the route. A study will need to be done to determine whether lower accelerations are needed for passenger comfort or if the design must be abandoned altogether

2. There is concern regarding interference between the magnetic field of the linear induction motor and the magnetic field from the levitation system. While it is likely that the frequency of the magnetic field generated by the LIM is so high that the magnetic field produced by the Halbach array is unaffected, further study is needed to confirm that interference does not lead to losses or other unintended effects.

Energy Cost Model

6.1 Overview

The total energy consumption of a Hyperloop pod can be calculated from the energy needed to accelerate and decelerate from and to rest, the energy needed to overcome losses to aerodynamic and magnetic drag, and the energy expended to maintain pressure in the tube at 100 Pa as pods enter and leave the tube.

6.1.1 Assumptions & Variables

We will make the following assumptions to simplify our analysis.

1. The pods accelerate at 1g, a value routinely done on commercial sedans and suitably comfortable for the average person
2. The tube is sealed at all times except when a pod enters or leaves the tube. In this scenario, a volume of air equal to an integer multiple, N_1, of the volume of tube which the pod occupies enters the tube. The air is at atmospheric pressure and we assume $N_1 = 4$.
3. For any given route, there is a pod entering and departing at each end of the tube and there are two tubes for each direction. Thus, a second multiplier, $N_2 = 4$, is added to assumption 2 above.
4. The electric efficiency, η, of the LIM is 0.8
5. The electric efficiency, γ of the vacuum pump is 0.5
6. The time between pods departing/arriving is 2 minutes, as described in the Hyperloop white paper
7. The drag coefficient of the pod is 0.3, similar to that of a hemisphere body with reduction to account for more streamlined shape of pod.
8. The air inside of the tube behaves as an ideal gas at T_a =300 K and P_a =100 Pa

Table 6.1: Variables in energy cost analysis

Variable	Value	Description
a_p	1g	Acceleration/deceleration of pods (g)
t_p	2	Time between pods (min)
N_1	4	Multiplier of volume of air entering tube (-)
N_2	4	Multiplier of volume of air entering tube (-)
η	0.8	Electric efficiency of LIM (-)
γ	0.5	Electric efficiency of vacuum pump (-)
ΔP	101225	Pressure difference between ambient and tube air (Pa)
ρ	0.0015	Air density inside tube (kg/m^3)

6.2 Acceleration/Deceleration

Kinematic relations can be used to derive the energy expended to accelerate & decelerate.

$$v_f = v_0 + a_p t \tag{6.1}$$

$$d = \frac{1}{2} a_p t^2 \tag{6.2}$$

$$E = \frac{Fd}{\eta} = \frac{1}{\eta} m_{pod} \cdot a_p \cdot d \tag{6.3}$$

The final velocity v_f is simply the cruise speed of Hyperloop, 724 km/hr (450 mph), and the initial velocity v_0 is 0. We can then solve equations 6.1-6.3 sequentially to find that it takes a total of 505 MJ to accelerate/decelerate the Hyperloop pod from/to rest at $1g$ of acceleration.

6.3 Drag

6.3.1 Aerodynamic

The drag equation is written as

$$F_D = \frac{1}{2}\rho c_D A_f U^2 \tag{6.4}$$

where c_D is the pod drag coefficient, ρ is the air density, A_f is the pod frontal area, and U is the pod speed. The frontal area A_f is $1.4m^2$ from the Hyperloop white paper, the pod speed is $201.15\frac{m}{s}$, & the air density is derived from the ideal gas law

$$PV = nRT \implies \rho = \frac{n}{V} = \frac{P}{RT} \tag{6.5}$$

where P is the pressure in the tube, V is the volume of the tube, n is the number of moles of gas, R is the universal gas constant, and T is the temperature in the tube. Here we assume $P = 100$ Pa and $T = 30°$C. Substituting these values into Equation 6.5 gives a tube air density of $\rho = 0.0015\frac{kg}{m^3}$. Substituting the values into equation 6.4 gives a drag force of 9.7 N. Then, the energy loss to drag per km is expressed as

$$E^A_{drag} = F_D * 1000m = 0.01\frac{MJ}{km} \tag{6.6}$$

6.3.2 Magnetic

In section 4.4, we derived the lift/drag ratio for a passive maglev system using a Halbach Array

$$\frac{L}{D} = \frac{1}{k\delta}\left(\sqrt{1 + \frac{k^4\delta^4}{4}} - \frac{k^2\delta^2}{2}\right)^{\frac{1}{2}} \tag{6.7}$$

where k is the wavenumber of the Halbach Array and δ is the skin depth of the conductor as we saw previously. In section 4.3 we found the lift to drag ratio for a Halbach Array with a wavelength of 0.5m moving along an aluminum track to be 19.5. We can calculate the drag force as

$$F_D = \left(\frac{L}{D}\right)^{-1} \cdot m_{pod}g \tag{6.8}$$

where we have used the fact that the lift force is equal to the weight of the pod. Substituting in the mass of the pod, we get a magnetic drag force of 5.4 kN. Then, the energy loss to magnetic drag per km is

$$E^M_{drag} = F_D * 1000m = 5.09\frac{MJ}{km} \tag{6.9}$$

The total energy to overcome aerodynamic and magnetic drag is then

$$E_{drag} = \frac{E^A_{drag} + E^M_{drag}}{\eta} = 6.38\frac{MJ}{km} \tag{6.10}$$

6.4 Vacuum Pumps

The volume of air that enters the tube is simply the volume of tube that a pod occupies

$$V_{air} = N_1 \cdot N_2 \cdot L_{pod} \cdot A_{tube} \tag{6.11}$$

where L_{pod} is the length of the pod and A_{tube} is the inner cross-sectional area of the tube. These values were solved for in previous sections so we can substitute them into Equation 6.11 and find that the volume of air entering the tube per pod is $6254.86m^3$. Then, if we know the time t between pods we can calculate the volumetric flow rate into the tube.

$$\dot{V}_{air} = \frac{V_{air}}{t} \tag{6.12}$$

From the Hyperloop white paper, the time between pods is 2 min which gives a volume flow rate of 3127.43 m^3/min. The energy cost per min operation of the vacuum pumps is then

$$\dot{E}_{pump} = \frac{\Delta P \dot{V}_{air}}{\gamma} = 633.15\frac{MJ}{min} \tag{6.13}$$

6.5 Risk Factors

1. The aerodynamic model is extremely simplistic - there may be additional losses through phenomena such as boundary layer separation, shock wave formation, or turbulence. A more comprehensive aerodynamic study is needed before the energy loss from drag can be used with certainty.

2. Our model of how air flows into the tube during entry/departure is a guess. Depending on the particular design of the system, air flow into the tube with pod departure/arrival can vary greatly.

3. We have assumed that the efficiency of the linear induction motor is 0.8 and vacuum pumps is 0.5. While this may be a reasonable approximation, the true efficiency depends on the specific design of the LIM and vacuum pump. An efficiency from manufacturer data-sheets should be referenced to create more accurate energy loss numbers.

Solar Energy

7.1 Overview

The Hyperloop Alpha white paper suggests powering the system using solar panels placed on top of the tubes. The solar panels would power the linear induction motors as the pod travels along the length of the tube while providing excess charge to battery packs to operate at night and extended periods of cloudy weather. While the Hyperloop white paper states that solar could produce "far in excess" of the energy needed to operate, here we investigate the validity of s by calculating the total solar energy that can be produced daily per kilometer of tube.

7.1.1 Assumptions & Variables

1. Solar irradiation values will be taken from an average over the Southwestern US. We focus on the southwestern US because the region has the highest solar irradiance and thus is likely to be a strong candidate for a potential future Hyperloop route.
2. The efficiency, α, of solar panels is 0.18
3. The average number of sunny days per year, c_f, in the Southwestern US is 250.
4. The solar panels will cover, $\lambda = 90\%$, of the length of the tubes
5. The market cost, C_{panel}, of a solar panel with efficiency α is \$130.24 per m^2

Table 7.1: Variables used in solar energy calculations

Variable	Value	Description
w	5.1	Width available for solar panels above tube (m)
λ	0.9	percentage of tube length allocated for solar panels (-)
A_{solar}	4593	Area of solar panels per km of tube (m^2)
I	6	Average solar irradiance during sunny days (kWh/m^2/day)
c_f	250	Average number of sunny days per year (-)
α	0.18	Efficiency of solar panel (-)
C_{panel}	130.24	Market cost of solar panel with efficiency α (\$/m^2)

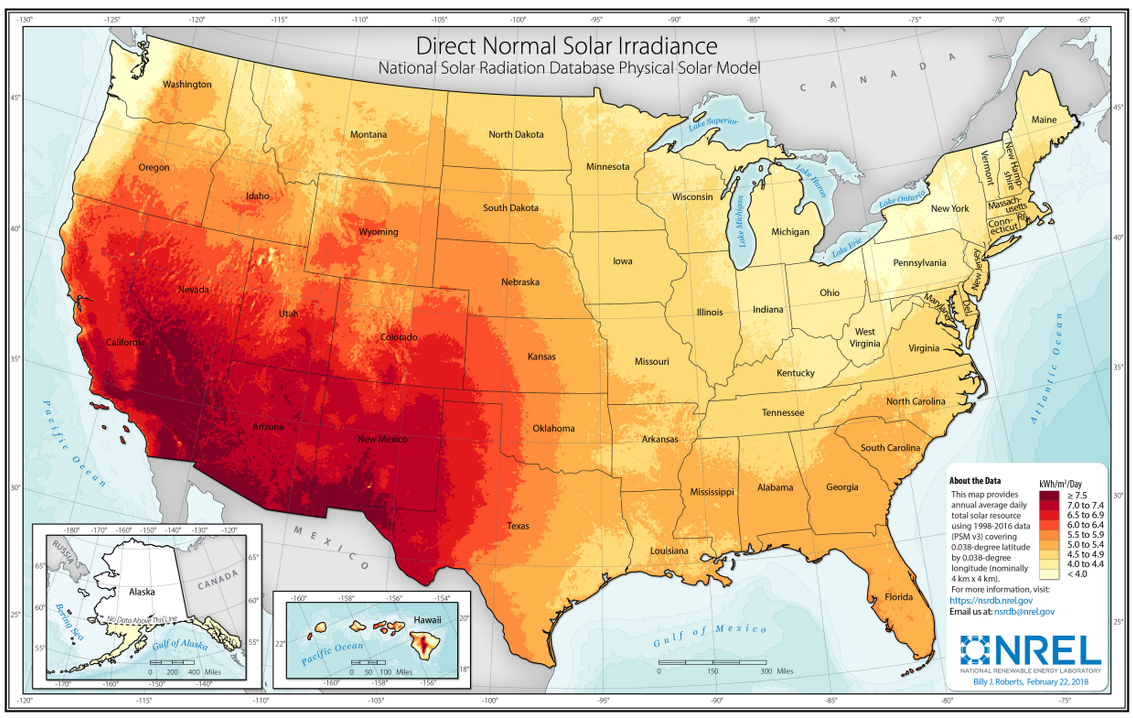

Figure 7-1: Average annual direct normal solar irradiance in the US [4].

7.2 Average Generation

A map of the average annual solar irradiation in the United States is shown in Fig. 7-1. The average solar irradiance was taken from historical US data from 1998-1996. The data reports the average annual direct normal solar irradiance and average annual direct horizontal solar irradiance. Of course, solar panels are neither normal to the sun or parallel to the sun but somewhere in between. We take the average of the normal & horizontal solar irradiance as a good approximation of the solar irradiance available to solar panels. The average solar energy generated daily per kilometer of route is calculated as

$$E_{solar} = 3.6 \cdot I \cdot A_{solar} \cdot \alpha \cdot \frac{c_f}{365} = 12232 \frac{MJ}{km - day} \tag{7.1}$$

The cost per km of solar panels is given directly by

$$C_{solar} = A_{solar} \cdot C_{panel} = \$598,000 \tag{7.2}$$

7.3 Risk Factors

1. Solar may not be a feasible solution for routes outside of the Southwestern US due to lower average annual solar irradiation and fewer days of sun per year. There are many busy corridors in other regions of the country, such as New York City/Washington D.C., and further study will be needed to figure out a way to power such routes.

2. Environmental factors such as wind, hail, and snow may require routine maintenance of solar panels. It will be critical to have a backup power source in the event that enough solar panels drop in efficiency that the total energy generated is not enough to power the volume of pods traveling through the tube.

Tube and Pylon Structure

8.1 Tube Overview

The Hyperloop consists of partially evacuated cylindrical tubes pumped down to 100 Pa (roughly 1/1000th of atmospheric pressure). The tubes must withstand stresses from the resulting pressure gradient and bending stresses induced by its own weight. Additionally, the tubes must be able to prevent buckling-induced collapse due to defects in manufacturing e.g. dent or ovality. The original Hyperloop Alpha white paper suggests a steel tube with a nominal thickness between 20-23mm, supported by pylons at an average spacing of 30m. Because the fixed cost of the tube dominates the overall cost of the Hyperloop system, we will go to lengths in the following sections investigating the fundamental equations which drive the design of the tube and explore design optimization to minimize cost.

8.1.1 Assumptions & Variables

Although the tube thickness calculated in the Hyperloop white paper is large enough to withstand a 1 atm pressure gradient, real world considerations must be taken into account. One of the prominent risk factors with a sealed tube on the order of hundreds of miles long is that any individual with a firearm could shoot holes into the structure, compromising the entire system. Our initial analysis found that - assuming a minimum steel tube thickness of 25mm to withstand repeated projectile impact - concrete is a more cost-effective material (see A-1). Thus, in our analysis we will make the following assumptions:

1. The tube is made of concrete, with a compressive yield strength of 34.5 MPa and tensile yield strength of 5 MPa
2. The tube can be modeled as a thin-walled pressure vessel
3. The minimum tube thickness necessary to withstand projectile impact is 100mm
4. Each tube section behaves as a beam simply supported by adjacent pylons

Table 8.1: Variables used in tube design analysis

Variable	Value	Description
D_i	2.55	Inner diameter of tube (m)
σ_y^C	34.5	Concrete compressive yield strength (MPa)
σ_y^T	5	Concrete tensile yield strength (MPa)
ΔP	0.1	Pressure difference across tube (MPa)
t_{min}	100	Minimum allowable thickness of concrete tube
S	3	Design safety Factor
g	9.8	Gravitational acceleration on Earth (m/s^2)
ρ_c	2900	Density of concrete (kg/m^3)
C_{con}	1000	Material cost of concrete ($/tonne)

8.2 Tube Design

We will use cylindrical coordinates (r, θ, z) to exploit the geometry of the tube. The Cauchy stress tensor in cylindrical coordinates is written as

$$\begin{bmatrix} \sigma_{rr} & 0 & 0 \\ 0 & \sigma_{\theta\theta} & 0 \\ 0 & 0 & \sigma_{zz} \end{bmatrix} \tag{8.1}$$

where we have made use of the fact that our coordinate axes align with the principal directions to cancel out the shear stress elements (off-diagonal components). Because the tube undergoes multiple loads in different directions, it is necessary to combine the different stress components in the tube into a single stress and evaluate for failure. In this analysis, we will use the von Mises equivalent stress, σ_v

$$\sigma_v = \sqrt{\frac{1}{2} \cdot [(\sigma_{rr} - \sigma_{\theta\theta})^2 + (\sigma_{\theta\theta} - \sigma_{zz})^2 + (\sigma_{zz} - \sigma_{rr})^2]} \tag{8.2}$$

where $\sigma_{rr}, \sigma_{\theta\theta}, \sigma_{zz}$ are the principal stresses given by the diagonal elements of the Cauchy stress tensor. It is important to note that in bending, the section of the tube above the neutral axis will undergo compression (-σ_{zz}) and the section below will undergo tension (+σ_{zz}). Thus, we will have two von Mises stresses, one for each direction of σ_{zz}. Thus, the two von Mises failure criteria are

$$\sigma_v^C \leq \frac{\sigma_y}{S} \tag{8.3}$$

$$\sigma_v^T \leq \frac{\sigma_y^T}{S} \tag{8.4}$$

where σ_v^C is the von Mises stress with σ_{zz} in compression, and σ_v^T is the von Mises stress with σ_{zz} in tension.

8.2.1 Pressure Loads

There are three stresses acting on the tube: the hoop stress (σ_h), the longitudinal stress (σ_l), and the radial stress (σ_r). It is important to note here that the longitudinal stress is a compressive stress and that the radial stress, though not shown in the free body diagram, arises simply as a result of the external pressure acting everywhere normal to the surface of the tube. The three stresses are expressed as

$$\sigma_h = \frac{\Delta P \cdot R}{t} \tag{8.5}$$

$$\sigma_l = -\frac{\Delta P \cdot R}{2t} \tag{8.6}$$

$$\sigma_r = \Delta P \tag{8.7}$$

where R and t are the inner radius and thickness of the tube, respectively.

8.2.2 Self-Loading

The other load acting on the tube is the self weight and this induces bending stresses. Euler-Bernoulli beam theory gives the following expressions for the maximum bending moment and bending stress in the tube section

$$m = \rho_c \cdot \frac{\pi}{4} \cdot ((D_i + \frac{2t}{1000})^2 - D_i^2) \tag{8.8}$$

$$M_{max} = \frac{mgL^2}{8} \tag{8.9}$$

$$\sigma_{max} = \frac{M_{max} R_o}{I} \tag{8.10}$$

where m is the mass per meter of tube, L is the spacing between pylons, R_o is the outer radius of the tube, and I is the second moment of area of the tub. As mentioned previously, bending creates both tensile and compressive stresses in the axial direction. We can now calculate the state of stress in the tube. The principal stresses are expressed as

$$\sigma_{rr} = \sigma_r \tag{8.11}$$

$$\sigma_{\theta\theta} = \sigma_h \tag{8.12}$$

$$\sigma_{zz} = \begin{cases} \sigma_{max} - \sigma_l, & \text{tension} \\ \sigma_{max} + \sigma_l, & \text{compression} \end{cases} \tag{8.13}$$

Substituting the principal stresses into the Equation 8.2 gives the von Mises equivalent stress. Assuming the thickness of the tube is fixed at $t = t_{min}$, we can calculate the maximum pylon spacing L_{max} that satisfies our failure criteria (Equations 8.3,8.4). However, we do not have to go to the maximum pylon spacing. A smaller pylon spacing will lead to more pylons for a given route, but the more pylons there are the less load each pylon will experience. Thus, there is a tradeoff between a lower cost per pylon but more pylons in aggregate. We will investigate the pylon design in the following section and combine the equations to determine the optimal pylon spacing.

8.3 Pylon Overview

The pylons' primary function is to support the tube along the length of the route. The forces acting on the pylons are primarily compression from the weight of the tube and bending stress induced by drag force from wind motion against the tube. The Hyperloop Alpha white paper suggests pylons constructed out of concrete due to the low cost per volume, with an average pylon height of 6m and spacing of 30m. We will keep the height of the pylons fixed, as this is largely determined by the geographic constraints along the specific route, and inspect how varying the diameter of the pylon affects its structural integrity. The goal, as with the design of the tube, is to investigate how governing equations can be used to minimize the pylon cost.

8.3.1 Assumptions & Variables

The pylons must also withstand vibrations/accelerations caused by earthquakes and stresses from thermal expansion/contraction of the tube. The Hyperloop Alpha white paper suggests the use of dampers at the tube-pylon interface to allow longitudinal slip for thermal expansion as well as dampened lateral slip to mitigate earthquake loads. To simplify our first-order analysis, we will assume that thermal loads are negligible with the use of dampers as suggested in the Hyperloop white paper. Additionally, we will treat earthquake loads as static (simple lateral acceleration) and make the assumption that the normal modes of the structure are outside the range of excitation frequencies of the earthquake. We make the following assumptions in our analysis:

1. Stresses from thermal expansion/contraction are negligible
2. The normal modes of the structure are outside the range of excitation frequencies from earthquakes i.e. no resonance
3. Earthquakes create a peak ground acceleration, a_{PG}, of 1g (See A-6)
4. The pylon is modeled as a concrete cylinder, with a compressive yield strength of 34.5 MPa and a tensile yield strength of 5 MPa
5. The height of the pylon is 6m, as specified in the Hyperloop white paper
6. The pylon is fixed to the ground and free to translate at the interface with the tube
7. The pylon behaves as a cantilevered beam fixed to the ground and free at the tube for lateral loads e.g. wind forces
8. The pylons extend below the ground for a distance equal to the length above ground i.e. 6m
9. The drag coefficient of the tube, $c_{D,tube}$, is 1.25 [9]
10. Wind blows perpendicular to the tube at a maximum speed of 200 km/h

Table 8.2: Variables in pylon design analysis

Variable	Value	Description
H	6	Height of column (m)
K	1	Column effective length factor (-)
E	40	Young's Modulus of concrete (GPa)
a_{PG}	1	Peak ground acceleration (g)
U	200	Wind speed (km/h)
$c_{D,tube}$	1.25	Drag coefficient of tube (-)
ρ_{amb}	1.225	Ambient air density (kg/m^3)

8.4 Pylon Design

8.4.1 Lateral Wind Loads

Once again we will use a cylindrical coordinate system (r, θ, z) to exploit the geometry of the pylon. The other load acting on the pylon are lateral wind forces. These wind forces can be calculated from the drag equation

$$F_D = \frac{1}{2}\rho_{amb} c_D A_f U^2 \tag{8.14}$$

where A_f is the tube frontal area. The frontal area is simply the product of the outer tube diameter, $D_o = D_i + 2t$, and tube span, L (spacing between pylons). The drag force on the tube induces bending stresses in the pylons. We can once again apply equations from Euler-Bernoulli beam theory

$$M_I = F_D \cdot H \tag{8.15}$$

$$\sigma_{bending,I} = \frac{M_I \cdot R_p}{I} \tag{8.16}$$

where I is the area moment of inertia of the pylon, given by $\frac{\pi R_p^4}{4}$ for a circular cross section.

8.4.2 Lateral Earthquake Loads

Historical data from the United States Geological Survey indicate typical peak ground accelerations of 1g in the state of California [10]. As stated in assumption 3, we will use a peak ground acceleration of 1g in our model. Typically in seismic analysis, the dynamic response of a structure to ground acceleration is represented by an equivalent static distribution of forces at points along the length of the structure. To simplify our analysis, we will assume that there is only one force, F_E, from the mass of the tube supported by the pylon accelerating at the peak ground acceleration, a_{PG}

$$F_E = wL \cdot a_{PG} \tag{8.17}$$

where the w is the mass per meter of tube, L is the spacing between pylons, and the product wL is the total mass of tube supported by the pylon. Similar to our analysis of wind loads in the previous section, the pylon acts as a cantilevered beam with the force of the accelerating tube acting on one end. The equations from Euler-Bernoulli beam theory give the resulting bending moment and stress

$$M_{II} = F_E \cdot H \tag{8.18}$$

$$\sigma_{bending,II} = \frac{M_{II} \cdot R_p}{I} \tag{8.19}$$

Combining the bending stress from lateral wind loads, $\sigma_{bending,I}$, with the bending stress from earthquake loads calculated above gives the total bending stress, $\sigma_{bending,T}$, acting on the pylon

$$\sigma_{bending,T} = \sigma_{bending,I} + \sigma_{bending,II} \tag{8.20}$$

8.4.3 Compressive Loads & Buckling

The compressive stress in the pylon is given by

$$\sigma_c = \frac{F}{A} = \frac{mgL}{\pi R_p^2} \tag{8.21}$$

where m is the mass per meter of tube, g is gravitational acceleration, L is the span of the pylons, and R_p is the radius of the pylon. The state of stress in the pylon can now be expressed as

$$\sigma_{rr} = 0 \tag{8.22}$$

$$\sigma_{\theta\theta} = 0 \tag{8.23}$$

$$\sigma_{zz} = \begin{cases} \sigma_{bending,T}, & \text{tension} \\ \sigma_{bending,T} + \sigma_c, & \text{compression} \end{cases} \tag{8.24}$$

Before we define the von Mises failure criteria, we must derive the buckling equations. The load a column can withstand before it undergoes buckling is given by Euler's critical load

$$P^* = \frac{\pi^2 EI}{(KH)^2} \tag{8.25}$$

where P^* is the maximum load before buckling occurs and I is the area moment of inertia of the column. The variable K depends on the boundary conditions of the column. As mentioned in our assumptions, the pylon is modeled as fixed to the ground on one end and free to translate at the other end. This is done so that the tube is not rigidly fixed at any one point, which helps alleviate stresses due to thermal expansion and vibrations. With this set of boundary conditions, $K = 1$, as listed in Table 8.2. Equation 8.25 can be rewritten in terms of the critical stress

$$\sigma^* = P^* A = \frac{\pi^2 E}{(L_e/r_g)^2} \tag{8.26}$$

where σ^* is the stress at which the column buckles, A is the column cross sectional area, L_e is the effective column length, r_g is the radius of gyration. The stress the column can withstand before it buckles scales inversely with the slenderness ratio, L_e/r_g. When the critical stress falls below the compressive yield strength of concrete, buckling becomes the primary loading scenario we must design for. We can calculate the von Mises equivalent stress, as defined in Equation 8.2, by substituting the principal stresses calculated in Equations 8.22-8.24. The von Mises failure criteria is then

$$\sigma_v^T \leq \frac{\sigma_y^T}{S} \tag{8.27}$$

$$\sigma_v^C \leq \begin{cases} \dfrac{\sigma^*}{S}, & \sigma^* \leq \sigma_y^C \\ \dfrac{\sigma_y^C}{S}, & \text{otherwise} \end{cases} \tag{8.28}$$

where σ_v^T is the von Mises stress with σ_{zz} in tension and σ_v^C us the von Mises stress with σ_{zz} in compression.

8.5 Optimization

We have laid out expressions for the von Mises stresses in the tube and pylon as a function of the pylon spacing, L, and the pylon radius, R_p. Since we set the tube thickness, t, to the minimum value $t_{min} = 100mm$, these are the only free parameters driving the design of the tube and pylon structure. Once these parameters are computed, the geometry of the structure is known and a cost per km can be calculated based on the volume of concrete used in the structure.

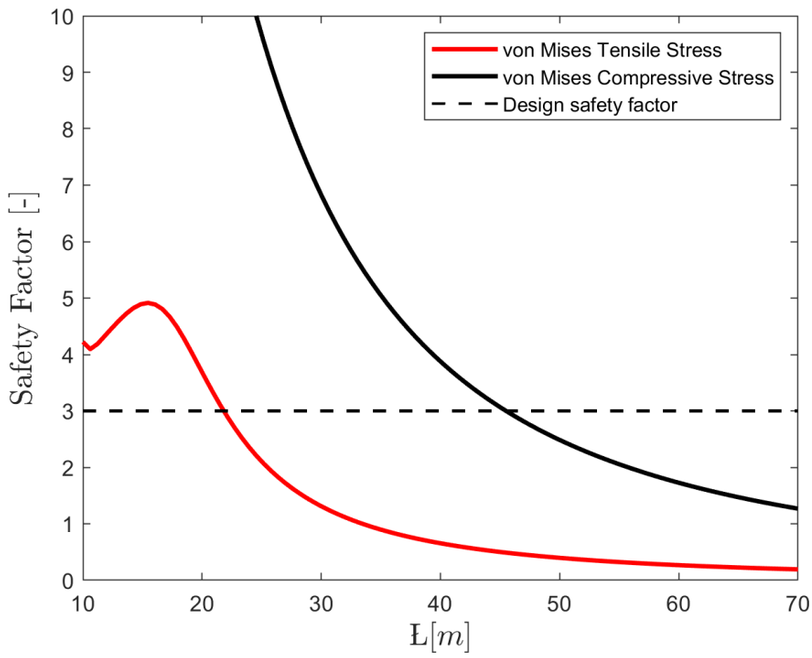

Figure 8-1: Tube tensile and compressive safety factor as a function of pylon spacing

In Fig. 8-1, the black curve is the safety factor of the von Mises compressive stress, σ_v^C, and the red curve is the safety factor of the con Mises tensile stress, σ_v^T, as the span L varies from 10m to 70m. The dashed black line indicates the design safety factor, $S = 3$. We can see from Fig. 8-1 that for a pylon spacing above $L = 22m$, the safety factor on the von Mises tensile stress drops below 3 which indicates failure. Thus, the suitable range of pylon spacing is between $L = 10m$ and $L = 22m$. Because the safety factor on the von Mises tensile stress is everywhere lower than the safety factor on the von Mises compressive stress - which is expected given that concrete is relatively weak in tension - we will only look at the tensile stress when analyzing the pylons.

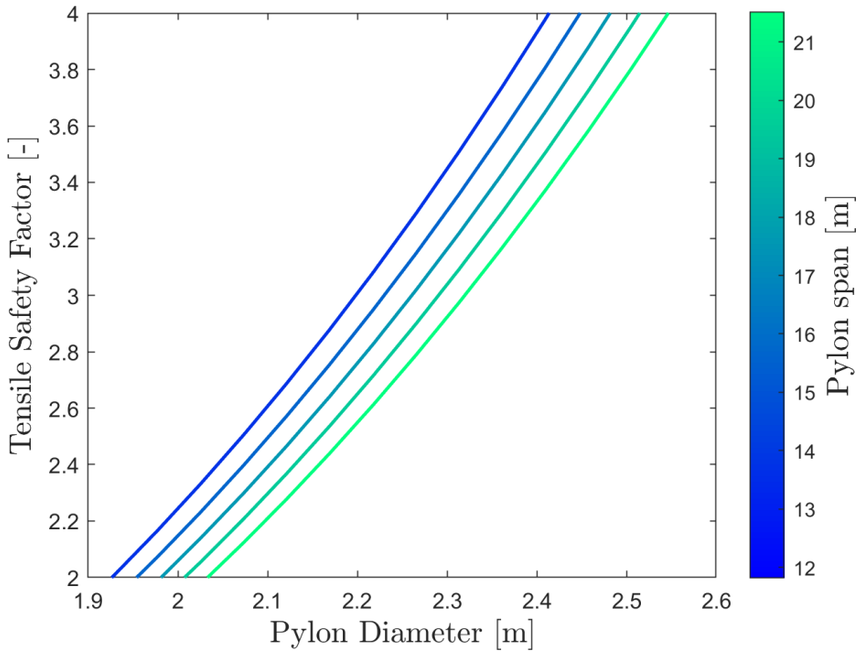

Figure 8-2: Pylon tensile safety factor as a function of pylon diameter and spacing

Figure 8-2 shows how the safety factor on the pylon von Mises tensile stress varies as a function of the pylon diameter and pylon spacing. The safety factor increases trivially with the pylon diameter. At a given safety factor, the pylon diameter must increase as the pylon spacing increases, which makes intuitive sense as a larger pylon spacing places greater loads on each pylon. We found from Fig. 8-1 that the range of pylon spacing which satisfies the von Mises failure criterion is $10m \leq L \leq 22m$. For each pylon spacing in that range, we can obtain the minimum pylon diameter necessary to obtain our design safety factor, $S = 3$, from Fig. 8-2. Thus, for each pylon spacing, L, we have a pylon diameter, D_p, which satisfies the von Mises failure criterion. The geometry is solved for and we can now calculate how the total cost of the structure varies as the pylon spacing, and consequently pylon diameter, varies.

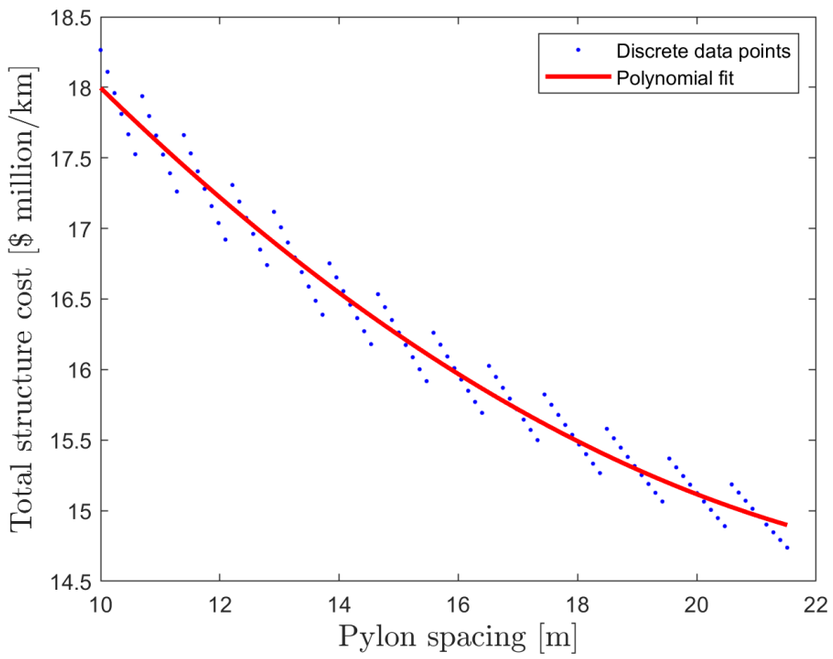

Figure 8-3: Tube and pylon cost per km in millions of US Dollars as a function of pylon spacing

From Fig. 8-3 we see that the total cost of the structure (tube and pylons) per km generally decreases as the pylon spacing increases. The blue points are the data points from our discretization and the red line is a 2^{nd} order polynomial fit. We can see that the blue points fluctuate up and down. The fluctuations occur because as the pylon spacing increases, the cost decreases monotonically until - at a critical spacing - the diameter of the pylon has to increase to support the additional load. At the point where the pylon diameter increases, the overall cost of the structure jumps and then proceeds to fall as pylon spacing increases until the diameter jumps once more. This behavior

occurs because of discretization in the numerical scheme. Realistically, the total cost of the structure decreases continuously with pylon spacing, as shown by the red curve. The lowest point on the curve indicates the cost minimization point. At this point, the pylon spacing is $L = 21.5m$, the pylon diameter is $D_p = 2.8m$, and the total structure cost is $14.8 million per km.

8.6 Risk Factors

We have made a number of assumptions in this analysis which need to be tested before confident

1. The size and cost of the structure will likely increase once thermal stresses and vibrations induced by seismic waves are included in the analysis.

2. The mass of the pod along with other tube structures such as solar panels, the maglev conductive track, and linear induction motors were not included in the mass of the tube. Include these elements will increase the stresses on the structure from self-loading.

3. The cost per km is likely to rise during the last few kilometers of the trip because there is no straightforward path into the city. The last few kilometers will likely involve many curves, dramatically increasing the overall cost. This may be mitigated by ending the route outside of the city, similar to airports, and letting passengers determine their mode of transport for the last few kilometers into the city.

Sample Routes

9.1 Overview

Now that we have derived the cost of each of the major subsystems of the Hyperloop, we can calculate the ticket cost for a Hyperloop between any two cities. For our analysis we will look at two of the busiest corridors in the southwestern US: the Los Angeles/San Francisco corridor and the Los Angles/Las Vegas corridor. Comparing the Hyperloop and airplane ticket cost for these routes will give us insight into the potential economic viability of the Hyperloop system.

9.2 Assumptions

1. We will not include land costs along the route, as this is highly dependent on geographical factors and the specific path taken between A and B. Additionally, the Hyperloop Alpha white paper claims that land costs can be largely mitigated by placing the tubes along the interstate, which we will assume to be true.
2. Station costs at ends of route, C_{st}, are \$250 million as stated in the Hyperloop white paper
3. Total vacuum pump costs, C_{vac}, are \$10 million as stated in the Hyperloop white paper
4. The cost per pod, C_{pod}, is \$1.35 million as stated in Hyperloop white paper
5. A capacity factor, c_f, of 0.5 is used to account for system operation below full capacity
6. A multiplier, M_1, of 2 is used to pay operating expenses and profit
7. A multiplier, M_2, of 2 to account for labor costs
8. An amortization period, T, of 20 years is used to recoup capital costs
9. An annual interest rate, r, of 5% on the capital borrowed

9.3 System Parameters

Table 9.1: Ticket cost parameters

Variable	Value	Description
v_{cruise}	450	Pod cruise speed (mph)
t_p	2	Time between pods (min)
N	28	Number of passengers per pod (m)
n_{trips}	1440	Number of one-way trips per day (-)
$V_{passengers}$	40320	Volume of passengers per day
E_{vacuum}	633.15	Daily energy cost to maintain tube vacuum (GJ/day)
E_{ad}	505	Energy to accelerate and decelerate (MJ)
E_{ms}	6.38	Energy per kilometer to maintain speed (MJ/km)
C_{pod}	1.35	Cost per pod (Million \$)
C_{tp}	14.8	Cost per km of tube and pylons (Million \$/km)
C_{LIM}	1.7	Cost per km of propulsion components (Million \$/km)
C_{lev}	0.184	Cost per km of levitation components (Million \$/km)
C_{solar}	0.598	Cost per km of solar panels (Million \$/km)
C_{vac}	10	Cost of vacuum pumps along route (Million \$)
C_{st}	250	Cost of stations at ends of route (Million \$)
T	20	Amortization period (years)
r	0.05	Annual interest rate (-)
CRF	0.08	Capital recovery factor (-)
cf	0.5	Capacity factor (-)
M_1	2	Multiplier to pay operating expenses and profit (-)
M_2	2	Multiplier to pay labor costs (-)

9.4 Los Angeles/Las Vegas

Table 9.2 shows that a route connecting Los Angeles and Las Vegas may not be economically favorable for Hyperloop, with a round trip ticket cost that is 2x the round trip airfare. On the other hand, Hyperloop offers the advantage of half the trip time. The flight time was calculated from Google Flights (See A-3). However, the system consumes more solar energy on average than it generates so the system may need connection to the grid for any energy consumption beyond what the solar panels produce. This will, of course, drive costs up.

Table 9.2: Route parameters for Los Angeles/San Francisco

Variable	Value	Description
d	431	Route distance (km)
E_{trip}	3253	Energy per one way trip (MJ)
E_{day}	5596	Total energy consumption per day over all trips (GJ/day)
E_{solar}	5272	Solar energy created daily (GJ/day)
$\boldsymbol{E_{excess}}$	**-324**	**Excess solar energy produced per day (GJ/day)**
C_{total}	7707	Total system fixed cost (Million $)
$\boldsymbol{C'_{total}}$	**15414**	**Total system fixed cost with multiplier for labor (Million $)**
C^*_{total}	24736	Total system fixed cost with capital recovery factor(Million $)
C_{ticket}	104.7	Round trip Hyperloop ticket cost ($)
$\boldsymbol{C'_{ticket}}$	**209.5**	**Round trip Hyperloop ticket cost with multiplier for operating cost and profit ($)**
C_{plane}	115	Round trip airplane ticket cost ($)
$\boldsymbol{C_{ratio}}$	**2.16**	**Ratio of Hyperloop to airplane ticket cost (-)**
t_{trip}	76.3	Hyperloop round trip travel time (min)
t_{plane}	141	Round trip flight travel time (min)
$\boldsymbol{t_{ratio}}$	**0.54**	**Ratio of Hyperloop to airplane travel time** (-)

9.5 Los Angeles/San Francisco

Table 9.3 shows that the economics for a route connecting Los Angles to San Francisco are worse than the previous route, with a round trip ticket cost that is 3x the round trip airfare. While the Hyperloop does offer a shorter travel time, taking 69% of the time an airplane would take (See A-3), the margin is slimmer than the LA-Vegas route. This indicates that Hyperloop may not be feasible for routes approaching 1000km, as airplanes are more efficient over longer distances. Another interesting point is that the system now produces enough solar energy to power the entire system, thanks to the longer route, but the longer route has also brought the fixed cost of infrastructure such that the economics of a longer route are less favorable for Hyperloop.

Table 9.3: Route parameters for Los Angeles/Las Vegas

Variable	Value	Description
d	611	Route distance (km)
E_{trip}	4400	Energy per one way trip (MJ)
E_{day}	7248	Total energy consumption per day over all trips (GJ/day)
E_{solar}	7474	Solar energy created daily (GJ/day)
$\boldsymbol{E_{excess}}$	**225**	**Excess solar energy produced per day (GJ/day)**
C_{total}	10840	Total system fixed cost (Million $)
$\boldsymbol{C'_{total}}$	**21680**	**Total system fixed cost with multiplier for labor (Million $)**
C^*_{total}	17397	Total system fixed cost with capital recovery factor(Million $)
C_{ticket}	147.3	Round trip Hyperloop ticket cost ($)
$\boldsymbol{C'_{ticket}}$	**294.6**	**Round trip Hyperloop ticket cost with multiplier for operating cost and profit ($)**
C_{plane}	97	Round trip airplane ticket cost ($)
$\boldsymbol{C_{ratio}}$	**3.04**	**Ratio of Hyperloop to airplane ticket cost (-)**
t_{trip}	108	Hyperloop round trip travel time (min)
t_{plane}	157	Round trip flight travel time (min)
$\boldsymbol{t_{ratio}}$	**0.69**	**Ratio of Hyperloop to airplane travel time** (-)

9.6 Risk Factors

The economics presented with these two sample routes should not be taken as factual evidence of Hyperloop's economic viability. There were many assumptions going into these calculations which must be reconciled before a bold conclusion can be made. Particularly,

1. We have not included land costs. If building the route along the interstate, as proposed in the Hyperloop white paper, is not as inexpensive as thought or not possible given geographical constraints the capital cost of Hyperloop could go up by a factor of 2 or 3.

2. Many variables were presented in the analysis which have a significant affect on the total ticket cost of the Hyperloop. Primarily, the multipliers M_1, M_2 for labor costs and operating costs/profit as well as the capacity factor cf drive the Hyperloop ticket cost. Further analysis should be done to determine the accuracy of these variables, as they may bring the total Hyperloop ticket cost up or down depending on how conservative our estimates are.

3. The risk factors mentioned in the preceding sections may lead to an increase in the cost of all of the subsystems, from tube and pylons to levitation and propulsion, as further research and analysis is done to iterate the design of the various subsystems.

Conclusion

This thesis presented a first-order model as a framework for analyzing the technical and economic aspects of a potential Hyperloop system. Given the tubes can only be evacuated to a finite pressure, roughly 1/1000th of atmospheric pressure, the Kantrowitz Limit placed a fundamental limit on the speed of the pod at a given pod to tube area ratio. We investigated three different sources of levitation - air bearings, passive maglev, and active maglev - and discovered that air bearings become unfeasible because of the required mass flow rate and consequently the volume of air that must be stored on the pod during a trip. Passive maglev was chosen over active maglev because of its inherent stability, low cost, and low power requirement. A basic framework for analyzing passive maglev was developed and used to calculate the magnetic drag.

A periodic propulsion concept was devised to minimize the cost of the stator-side of the linear induction motor. We calculated the average solar energy generated daily and found that it may be possible to produce enough solar energy to power the system. We then developed an optimization model to explore design trade-offs in the tube and pylon structure. Finally, analysis of each subsystem was combined to create a model to determine a Hyperloop ticket cost for any given route between two cities. The model allows for updated operating, labor, and material costs to be considered and conclusions made. From our analysis with our operating, labor, and material cost estimates, it appears that the Hyperloop may have the potential to be economically competitive with airplanes over modest distance routes i.e. below 1000km, but in addition a significant amount of further research and analysis is needed before a conclusion can be reached. The first-order models must be refined to include effects that were initially ignored, and risk factors must be addressed at each stage of the design process.

Future Research

Many simplifying assumptions were made in this analysis in order to construct a first-order model to determine the feasibility of Hyperloop. The following are areas of research that should be expanded on in order to improve the models developed here and come to a more rigorous conclusion on the technical and economic feasibility of Hyperloop.

11.1 Going Supersonic

A potential solution to overcoming the Kantrowitz Limit is placing a pump in front of the pod to move air accumulating upstream of the pod to a location further downstream. An analysis should be done to determine the mass flow rates necessary as a function of speed and whether commercially available pumps can achieve those mass flow rates. Theoretical analysis should be coupled with simulations (computational fluid dynamics) as supersonic flow in a tube may lead to the formation of shock waves which leads to losses and complicates the analysis. If it is possible to overcome the Kantrowitz Limit within a reasonable power consumption, a trade study must be done to weigh the benefits of supersonic travel against the costs (primarily infrastructure and power).

11.2 Structural Loading

Thermal fluctuations throughout the day will lead to expansion and contraction in different segments of the tube structure. Even without thermal fluctuations, the top segment of the tube is exposed to the Sun while the bottom segment is shaded which will lead to natural thermal stresses. The thermal stresses that arise in the tube must be included in the design and analysis of the tube structure. Thermal expansion joints should be investigated as a means to connect segments of the tube minimize thermal stresses. Vibrations caused by seismic waves are also a concern, especially considering California's precarious location along fault lines. Careful study should be done to determine how significant vibration is and how the use of dampeners can mitigate resonance and other vibration-induced failure modes.

11.3 Cost Modeling

The first-order cost analysis developed in this thesis needs serious iteration. In particular, a framework should be built to determine the optimal route between city pairs. This will help account for land costs, curves in the tube, "last-mile" routing, and elevation changes. Additionally, a tool should be developed to more accurately estimate the labor cost to build the massive Hyperloop infrastructure and research should be done to determine the percentage of full capacity the system will operate at, on average. Finally, special attention should be given on the feasibility of cost minimization by building the Hyperloop along the interstate. It is unclear whether local governments will allow private companies to build on the interstate without serious discussions and certification.

11.4 Passenger Comfort

One of the more critical factors in determining the success of a new technology is its reception by the public. The Hyperloop design analyzed in this thesis presents serious issues to passenger comfort. The cramped geometry of the pod suggested in the Hyperloop Alpha white paper is excellent for optimizing cost and performance but has little consideration for passengers. It is likely that the real world Hyperloop will need a much larger pod, and consequently tube, in order to provide passengers with space to move around. Periodic acceleration is also a clever way to minimize propulsion costs but may lead to nausea and irritation from passengers as they are constantly subjected to 1g of acceleration over several hundred kilometers. The tube will need curves with ample radius of curvature when making turns as the centripetal forces at 450 km/h will be extremely painful below a critical curvature. Finally, the idea of moving through a dark tube perfectly sealed from the rest of the world may be daunting to some. Ideas such as windows placed periodically along the tube are interesting but are a structural liability and introduce manufacturing complexity. Passenger comfort was largely neglected in this analysis but it is vital that a future, more rigorous study investigate ways to balance the trade-offs between passenger comfort and cost efficiency.

11.5 Rapid Tube Pressurization

Leaks in the tube are both a safety and performance concern. Even a small leak may grow larger as the massive pressure gradient across the tube stresses the material near the leak. The rapid pressurization of the tube may drive the system to a halt because of the sudden increase in air resistance and flow instability local to the leak. A study should be done to determine the growth of leaks in the tube, the critical leak size that will force the system to shut down, and potential ways to seal a leak before it reaches critical size.

11.6 Optimized System Design

In our design of the Halbach Array the decision was made to forego optimization of the magnet design in order to quickly determine a rough approximation for the magnetic drag force and cost of the system. A second iteration of this study should look into optimizing the magnet design, particularly because the magnetic drag is the dominant source of resistance in the system. A design which reduces the magnetic drag would greatly reduce the energy cost and thus the ticket cost of the Hyperloop for any given route. Design of the propulsion system was largely neglected in favor of using the linear induction motor design from the Hyperloop white paper. While this may be sufficient for a first-order model, a further study should derive the governing equations of linear induction motors and conduct design trade studies to determine whether the design proposed in the Hyperloop white paper can be optimized to dramatically reduce costs.

Acknowledgements

The author would like to thank Professor Alexander Slocum for his initial advice on analyzing transportation systems, extensive insight on concrete structures, and allowing the use of a basic framework he developed from his own analysis of Hyperloop during his work at the Office of Science and Technology Policy (OSTP).

References

[1] SpaceX. Hyperloop alpha. *SpaceX (Online Article)*, 2013.

[2] Adonios N. Karpetis Eric Chaidez, Shankar P. Bhattacharyya. Levitation methods for use in the hyperloop high-speed transportation system. *Energies*, 2019.

[3] Wikimedia Commons. Halbach array, 2010. https://en.wikipedia.org/wiki/File:Halbach2.svg.

[4] Y. Xie A. Lopez A. Habte G. Maclaurin Sengupta, M. and J. Shelby. The national solar radiation data base (nsrdb). *Renewable and Sustainable Energy Reviews*, 2018.

[5] A. Kantrowitz and C. Donaldson. Perliminary investigation of supersonic diffusers. *National Advisory Committee for Aeronautics*, 1945.

[6] Brian J Cantwell. *Fundamentals of Compressible Flow*. 2018.

[7] F Post, R and D Ryutov. The inductrack concept: A new approach to magnetic levitation. *American Institute of Aeronautics and Astronautics*, 1996.

[8] K. D. Bachovchin, J. F. Hoburg, and R. F. Post. Stable levitation of a passive magnetic bearing. *IEEE Transactions on Magnetics*, 49(1):609–617, 2013.

[9] Giancarlo Bruschi, Tomoko Nishioka, Kevin Tsang, and Rick Wang. Drag coefficient of a cylinder. 2003.

[10] U.S. Geological Survey. Seismic design maps, 2009. https://earthquake.usgs.gov/hazards/designmaps/pdfs/?code=AASHTOedition=2009.

Appendix

Concrete compressive strength (Mpa)	34.50	
Concrete tensile strength (Mpa)	5.00	
Concrete modulus of elasticity (Gpa)	40.00	
Pressure gradient (Mpa, atm)	0.10	1
Concrete density (kg/m^3)	2900.00	
Tube inner diamter (m)	2.55	
Tube thickness (mm)	100.00	
Tube outer diameter (m)	2.75	
Cross sectional area of tube shell (m^2)	0.83	
Tube volume per km (m^3)	833.08	
Area moment of inertia (m^4)	0.65	0.73
Pylon span (m)	21.50	
Mass per length of tube (kg/m)	2415.94	
Hoop stress (Mpa)	1.28	
Longitudinal stress (Mpa)	0.64	
Radial stress (Mpa)	0.10	
Maximum bending moment (N-m)	1368039.37	
Bending stress (Mpa)	2.57	
Tube stresses		
Total radial stress, sigma_r (Mpa)	0.10	
Total circumferential stress, sigma_c (Mpa)	1.28	
Total axial stress (tension), sigma_at (Mpa)	1.93	
Total axial stress (compression), sigma_ac (Mpa)	3.20	
Von mises stress (tension)	1.61	
Von mises stress (compression)	2.72	
% of tensile strength used	**32.11%**	
% of compressive strength used	**7.87%**	
Pylon diameter (m)	1.59	
Pylon height (m)	6.00	
Cross section area (m^2)	1.99	
Area moment of inertia (m^4)	0.31	
Pylon volume (m^3)	23.83	
Weight of pylon (tonne)	69.10	
Compressive stress (Mpa)	**0.51**	
Frontal area (m^2)	59.16	
Wind speed (km/h, m/s)	200.00	55.56
Air density at sea level (kg/m^3)	1.23	
Tube drag coefficient (-)	1.25	
Lateral force on tube (N)	139805.25	
Bending moment on pylon, M_wind (N-m)	838831.51	
Bending stress from wind load (Mpa)	**2.13**	
Pylon stresses		
Total radial stress, sigmap_r (Mpa)	0.00	
Total circumferential stress, sigmap_c (Mpa)	0.00	
Total axial stress (tension), sigmap_at (Mpa)	1.61	
Total axial stress (compression), sigmap_ac (Mpa)	2.64	
Von mises stress (tension)	1.61	
Von mises stress (compression)	2.64	
% tensile strength used	**32.26%**	
% compressive strength used	**7.65%**	
Cost		
Cost per tonne of concrete ($/tonne)	$1,000.00	
Pylons per km (-)	46.51	
Cost per pylon ($/pylon)	$69,097.67	
Total pylon cost per km ($/km)	**$3,213,844.90**	
Total tube cost per km	**$4,831,873.80**	
Total structure cost per km	**$8,045,718.70**	

Figure A-1: Trade study using concrete tubes and concrete pylons

Steel compressive strength (Mpa)	210.00	
Steel tensile strength (Mpa)	210.00	
Steel modulus of elasticity (Gpa)	200.00	
Pressure gradient (Mpa, atm)	0.10	1
Steel density (kg/m^3)	8050.00	
Tube inner diamter (m)	2.55	
Tube thickness (mm)	25.00	
Tube outer diameter (m)	2.60	
Cross sectional area of tube shell (m^2)	0.20	
Tube volume per km (m^3)	202.38	
Area moment of inertia (m^4)	0.16	0.17
Pylon span (m)	67.00	
Mass per length of tube (kg/m)	1629.16	
Hoop stress (Mpa)	5.10	
Longitudinal stress (Mpa)	2.55	
Radial stress (Mpa)	0.10	
Maximum bending moment (N-m)	8958783.25	
Bending stress (Mpa)	69.38	
Tube stresses		
Total radial stress, sigma_r (Mpa)	0.10	
Total circumferential stress, sigma_c (Mpa)	5.10	
Total axial stress (tension), sigma_at (Mpa)	66.83	
Total axial stress (compression), sigma_ac (Mpa)	71.93	
Von mises stress (tension)	64.37	
Von mises stress (compression)	69.46	
% of tensile strength used	**30.65%**	
% of compressive strength used	**33.08%**	
Pylon diameter (m)	0.85	
Pylon height (m)	6.00	
Cross section area (m^2)	0.57	
Area moment of inertia (m^4)	0.03	
Pylon volume (m^3)	6.81	
Weight of pylon (tonne)	54.82	
Compressive stress (Mpa)	**3.77**	
Frontal area (m^2)	174.32	
Wind speed (km/h, m/s)	250.00	69.44
Air density at sea level (kg/m^3)	1.23	
Tube drag coefficient (-)	1.25	
Lateral force on tube (N)	643630.66	
Bending moment on pylon, M_wind (N-m)	3861783.97	
Bending stress from wind load (Mpa)	**64.05**	
Pylon stresses		
Total radial stress, sigmap_r (Mpa)	0.00	
Total circumferential stress, sigmap_c (Mpa)	0.00	
Total axial stress (tension), sigmap_at (Mpa)	64.05	
Total axial stress (compression), sigmap_ac (Mpa)	67.82	
Von mises stress (tension)	64.05	
Von mises stress (compression)	67.82	
% tensile strength used	**30.50%**	
% compressive strength used	**32.30%**	
Cost		
Cost per tonne of steel ($/tonne)	$2,420.00	
Pylons per km (-)	14.93	
Cost per pylon ($/pylon)	$132,653.96	
Total pylon cost per km ($/km)	**$1,979,909.88**	
Total tube cost per km	**$7,885,127.08**	
Total structure cost per km	**$9,865,036.95**	

Figure A-2: Trade study using steel tubes and concrete pylons

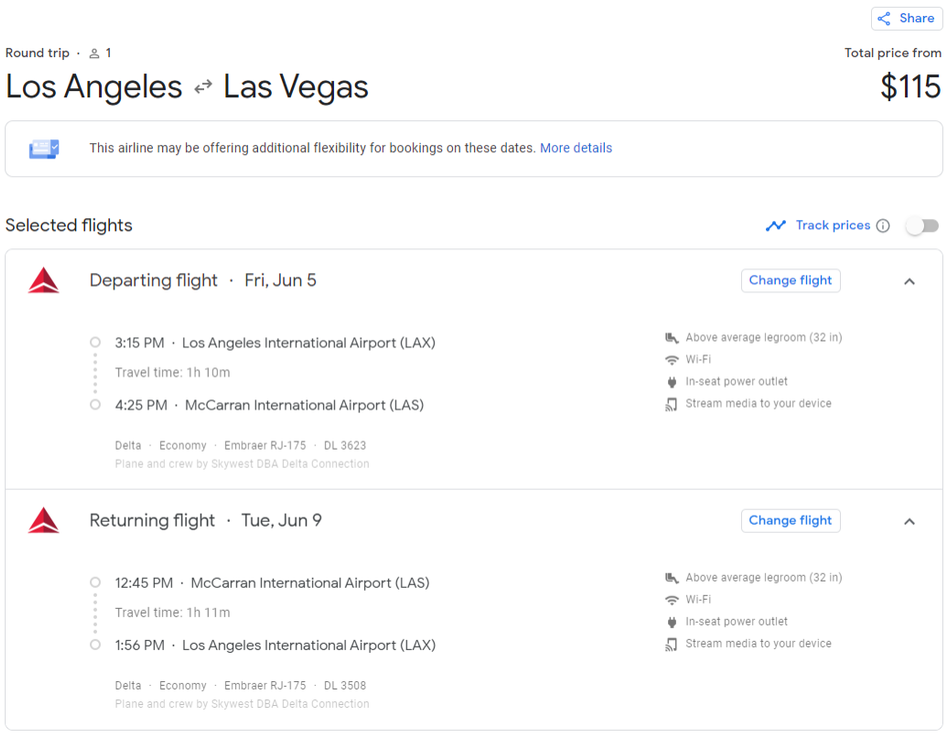

Figure A-3: Google Flights fare reference for round trip Los Angeles - Las Vegas

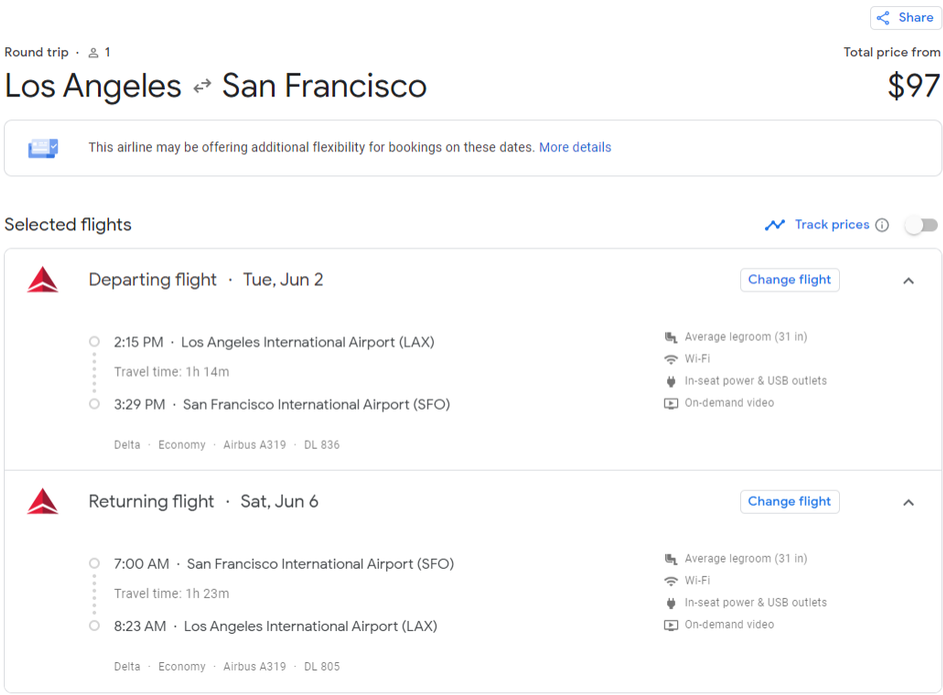

Figure A-4: Google Flights fare reference for round trip Los Angeles - San Francisco

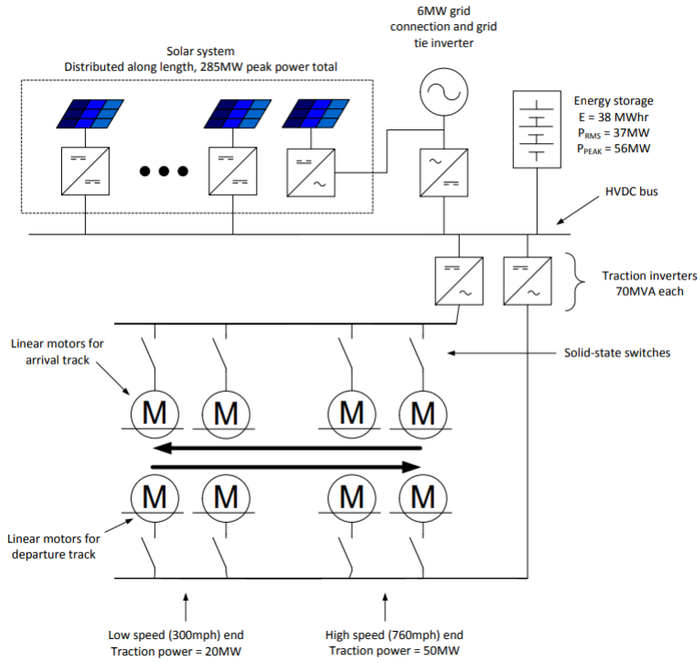

Figure A-5: Linear induction motor design proposed in Hyperloop Alpha white paper

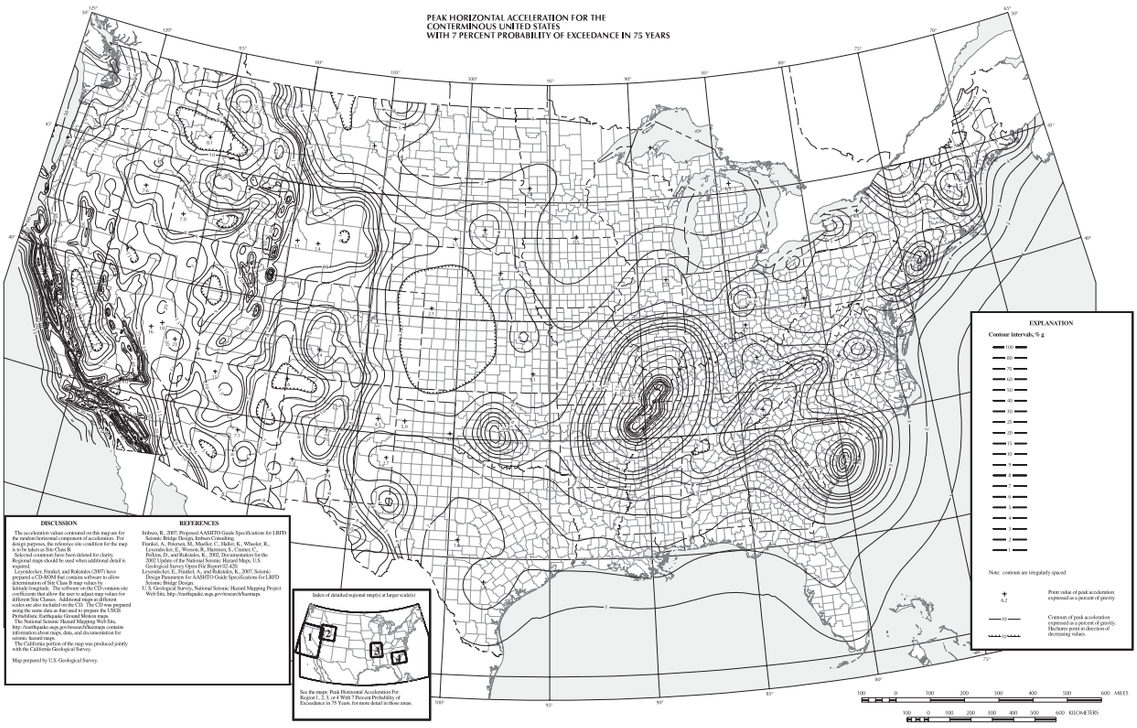

Figure A-6: Contour map of peak horizontal accleration in United States